11-28-2022

Cybersecurity and dynamic operation in practice: Equipment impacts and safety guarantees

Kip Nieman
Department of Chemical Engineering and Materials Science, Wayne State University, Detroit, MI

Dominic Messina
Department of Chemical Engineering and Materials Science, Wayne State University, Detroit, MI

Matthew Wegener
Department of Chemical Engineering and Materials Science, Wayne State University, Detroit, MI, gf8967@wayne.edu

Helen Durand
Department of Chemical Engineering and Materials Science, Wayne State University, Detroit, MI, helen.durand@wayne.edu

Recommended Citation

K. Nieman, D. Messina, M. Wegener & H. Durand, "Cybersecurity and dynamic operation in practice: Equipment impacts and safety guarantees," Journal of Loss Prevention in the Process Industries, vol. 81, 104898, Feb. 2023. https://doi.org/10.1016/j.jlp.2022.104898

Cybersecurity and Dynamic Operation in Practice: Equipment Impacts and Safety Guarantees

Kip Nieman, Dominic Messina, Matthew Wegener, and Helen Durand[a,*]

[a]*Department of Chemical Engineering and Materials Science, Wayne State University, Detroit, MI 48202.*

Abstract

Though dynamic operation of chemical processes has been extensively explored theoretically in contexts such as economic model predictive control or even considering the potential for cyberattacks on control systems creating non-standard operating policies, important practical questions remain regarding dynamic operation. In this work, we look at two of these with particular relevance to process safety: 1) evaluating dynamic operating policies with respect to process equipment fidelity and 2) evaluating procedures for determining the parameters of an advanced control law that can promote both dynamic operation as well as safety if appropriately designed. Regarding the first topic, we utilize computational fluid dynamics and finite element analysis simulations to analyze how cyberattacks on control systems could impact a metric for stress in equipment (maximum Von Mises stress) over time. Subsequently, we develop reduced-order models showing how both a process variable and maximum Von Mises stress vary over time in response to temperature variations at the boundary of the equipment, to use in evaluating how advanced control frameworks might impact and consider the stress. We close by investigating options for obtaining parameters of an economic model predictive control design that would need to meet a variety of theoretical requirements for safety guarantees to hold. This provides insights on practical safety aspects of control theory, and also indicates relationships between control and design from a safety perspective that highlight further relationships between design and control under dynamic operation to deepen perspectives from the computational fluid dynamics and finite element analysis discussions.

*Corresponding author: Tel: +1 (313) 577-3475; E-mail: helen.durand@wayne.edu.

1. Introduction

Dynamic operation of chemical processes has been a topic of interest for control for decades. For example, periodic operation of reactors has been considered Silveston (1987); Dermitzakis and Kravaris (2009), and dynamic operation can also be of importance in power plants Kim and Lima (2022). In the last decade or so, economic model predictive control (EMPC) Diehl et al. (2010); Ellis et al. (2014a) has been a control design of interest, as it is able to operate processes in a dynamic fashion. Specifically, it is an optimization-based control design that can explicitly optimize process economics. If a steady-state operating condition is not economically optimal, EMPC may not operate a process at steady-state. This may be particularly appealing in cases where constraints or economic metrics are time-varying Ellis and Christofides (2014); Gopalakrishnan and Biegler (2013), as then the control design is able to account for these changes with time and drive the closed-loop state along an optimal trajectory with respect to such objectives and constraints, rather than insisting on a steady-state tracking policy. Though many theoretical studies have demonstrated that EMPC is capable of maintaining closed-loop stability according to different notions (e.g., Heidarinejad et al. (2012); Griffith et al. (2017); Müller and Grüne (2016)), important practical considerations regarding its impacts on process equipment and design require further attention.

Equipment fidelity is critical and has motivated operations which avoid the degradation of equipment Wiebe et al. (2018). Prior work in our group Durand (2019a) has begun preliminary investigations into how EMPC could impact process equipment; however, even with consideration of integrating the design and control of processes under EMPC Oyama and Durand (2020b), our understanding of how EMPC interacts with equipment and process design remains incomplete.

While dynamic process operation can be set up by advanced control policies, another type of event which could cause dynamic operating policies for a system is cyberattacks. Cyberattacks represent an increasing threat to interconnected process systems. These threats are varied (in targeting strategy, level of sophistication, and motive) and can interact with control systems in many ways. Since the control systems are directly tied to the process itself, control actions (and thus cyberattacks) can directly affect process equipment. Such control actions can be manipulated

to a variety of ends, including covertly damaging process equipment to cause delays or to create an accident (as cyberattacks Cormier and Ng (2020) and dynamic operating policies have potential to damage process equipment Wang et al. (2019); Durand (2019b)). The potential severity of these consequences merit investigation into ways of detecting, preventing, and mitigating the consequences of cyberattacks.

Goals for cyberattacks on industrial systems may include, but not be limited to, sabotage of equipment, data alteration, and intellectual property theft motivated by financial gain Mahoney (2017), seeking to target vulnerabilities in manufacturing systems Tuptuk and Hailes (2018). Mahoney (2017) notes that cyberattack policies may change over time to take advantage of an increasingly digitized and data-driven manufacturing sector based on wired/wireless network connections. The integration of physical processes, control designs, embedded systems and communication networks in a cyber-physical system (CPS) framework Ding et al. (2018), though it advances process operation and enhances the capability to control the process, makes these connected systems vulnerable to cyberattacks which can cause changes to the CPS components (sensor measurements, signals to actuators, controller code) consequently affecting the system dynamics.

Several approaches to analyzing a system to identify and understand cyberattacks have been developed. These include information technology approaches where specific computer system layouts are combined with risk detection or analysis methods Candell et al. (2014); Perales Gomez et al. (2021); Wu et al. (2018). Industry typically addresses cybersecurity in similar terms, while also applying best-practices or standards to develop an organizational strategy to ensure cybersecurity Byres and Lowe (2004). Industry is interested in securing cyber-physical systems because attacks can potentially, unbeknownst to operators, affect the structural integrity of produced parts Wells et al. (2014) and process control systems Khorrami et al. (2016).

Prior work in our group has focused on a variety of issues surrounding cybersecurity, including investigating the modeling of equipment in controller design, which could yield benefits that include safer plants Durand and Wegener (2020); Nieman et al. (2020), and developing control theory that enables characterization of control designs which could guarantee that certain conditions on safety of a process hold even in the presence of cyberattacks. However, these topics have not been investigated

thoroughly from a practical perspective to work toward understanding the industrial relevance of this research, and whether it would add any layers of security to plant attack-handling strategies or not. For example, our prior work addressing process and equipment design in a cybersecurity context has been limited, focusing on several small-scale simulations of processes described by ordinary differential equations and a high-level discussion of how a more rigorous computational fluid dynamics and finite-element analysis simulation might be used in exploring cyberattack impacts on processes. Furthermore, though our work has developed theory for cyberattack-resilient control design, an appropriate method for obtaining the parameters of the control laws which enable these theoretical guarantees is unclear. As noted in Oyama et al. (2021), developing a controller intended to provide resilience against cyberattacks without checking that the theoretical conditions are met may not be beneficial, because it may not actually have cyberattack-resilience guarantees and therefore there may be vulnerabilities which an attacker could exploit.

Motivated by these gaps in the practical use of cyberattack-handling strategies for chemical process systems to prevent accidents at chemical plants, and gaps in our understanding of how other dynamic operating policies might impact process equipment, this work first develops a detailed discussion of how the impacts of cyberattacks and other potentially dynamic operating policies on process equipment might be evaluated using computational fluid dynamics and finite element analysis through demonstration using a steam methane reforming reactor. Subsequently, we compare concepts for developing simulation studies for an advanced control strategy when it is desired to demonstrate the controller's safety properties. The advanced control strategy for which we will perform this analysis has been modified to integrate it with cyberattack detection policies so that, if certain theoretical guarantees hold with respect to the modified control law, certain types of undetected attacks cannot pose a safety hazard (e.g., Oyama and Durand (2020a)). In future work, we would like to be able to demonstrate the operation of such cyberattack-resilient control and detection strategies with simulation studies. We consider the investigation of simulation strategies for the control law that the cyberattack-resilient forms are derived from to be a step toward simulating the cyberattack-resilient controllers.

2. Computational Fluid Dynamics and Finite Element Analysis: A Framework for Comprehensive Testing of Dynamic Operation Impacts

We previously suggested that computational fluid dynamics (CFD) and finite element analysis (FEA) simulations could be used as a cyberattack test bed Nieman et al. (2020). Such simulations could be useful because the equations involved are complicated, and simulations may demonstrate how a system and controller will respond to different conditions. There is a limited amount of research focusing on using CFD and FEA methods to analyze cyberattacks. However, CFD and FEA simulation methods are widely used to analyze components of a variety of systems in both industry and research settings Anderson and Wendt (1995) including, for example, piezoelectric disks Meesala et al. (2020) and smart tires Behroozinia et al. (2019). Therefore, these modeling strategies are appropriate to model process equipment as well. This section presents an exploration of utilizing CFD/FEA for modeling and examining the equipment-control interface in depth.

Specifically, this section uses computational fluid dynamics and finite element analysis to study a steam methane reforming (SMR) reactor under a cyberattack. This builds on previous work Lao et al. (2016); Tran et al. (2017a), which simulated fluid flow through the reactor, to also include a structural analysis of the pipe wall material. Here, we specifically consider an attack that targets a sensor and alters the sensor measurements to be different values in an effort to damage process equipment. The simulation was created using ANSYS Workbench, which includes leading industry CFD/FEA software capable of simulating a wide variety of phenomena. Both FEA and CFD involve subdividing a region into elements, which are then used to numerically integrate the coupled partial differential equations involved in fluid dynamics (in the case of CFD) and solid mechanics (in the case of FEA).

We close with an extension of the simulation of the SMR under a cyberattack, which specifically explores how advanced control policies (which have a potential to create dynamic effects) could impact process equipment. To do this, the simulation results are used to create reduced-order data-driven autoregressive with exogenous terms (ARX) models to relate control inputs to equipment stress in a computationally tractable way. These models are then applied in an IPOPT code Wächter and Biegler (2006) with ADOL-C Walther and Griewank (2009) (using code from Walther (2010)

for integrating them in C++) to simulate the process under model predictive control (MPC), which is a control algorithm that optimizes the future trajectory of the process using estimates from a process model. These simulations indicate that closed-loop MPC simulations, combined with efficient reduced-order models, can give a useful test bed environment for predicting the response of a process to cyberattacks and other dynamic operating policies.

2.1. CFD/FEA Evaluation Preliminaries

2.1.1. Steam Methane Reforming (SMR) Reactors

One method of the production of hydrogen is through using a specially designed reactor called a steam methane reformer (SMR), which consists of a number of packed tubes located in a chamber containing burners to apply heat to the endothermic reaction. A simplified schematic of an SMR reactor is shown in figure 1. There is no mixing of the reaction and combustion streams and they interact through heat conduction through the tube walls. In this work it is assumed that the tubes are packed with nickel oxide catalyst particles over an alpha alumina support ($Ni/\alpha - Al_2O_3$), which is necessary to enable the reaction to form hydrogen.

The main reactions occurring in the tube-side reaction are as follows Xu and Froment (1989):

$$CH_4(g) + H_2O(g) \rightleftharpoons CO(g) + 3H_2(g) \tag{1a}$$

$$CO(g) + H_2O(g) \rightleftharpoons CO_2(g) + H_2(g) \tag{1b}$$

$$CH_4(g) + 2H_2O(g) \rightleftharpoons CO_2(g) + 4H_2(g) \tag{1c}$$

2.1.2. Von Mises (Equivalent) Stress

In the mechanics of solids, stress (typically denoted as σ) is a quantity that represents the amount of force F applied over a given area A. In a single dimension, this can be represented simply as $\sigma = F/A$; however, in three dimensions stress is denoted as a tensor with nine terms, as in figure 2. These components, denoted as σ_{ij}, represent the stress on plane i in the direction j. For example, σ_{xy} represents the stress on the x-plane in the y-direction. If $i = j$, the component is known as normal stress, and if $i \neq j$, the component is known as shear stress.

The von Mises stress σ_{VM} is a scalar quantity that can be used as a yield criterion and is applicable to ductile and isotropic materials ANSYS (2022). It is a function of the stress state of

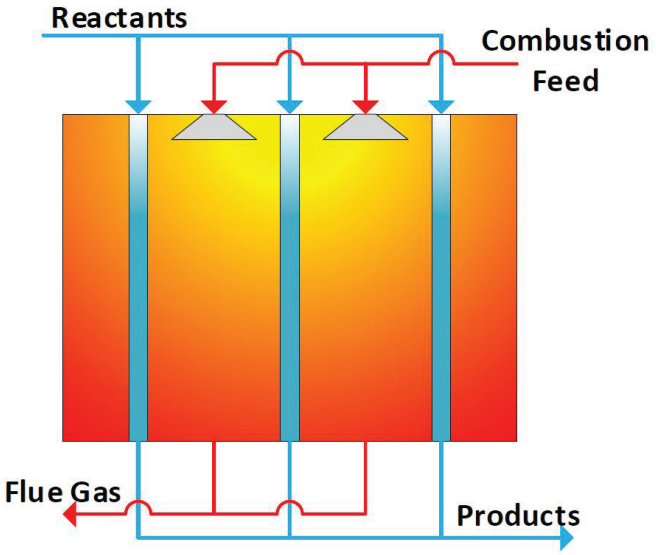

Figure 1: Simplified schematic of a steam methane reforming reactor (note that a real SMR would have many more tubes than what is shown, and the figure is not to scale).

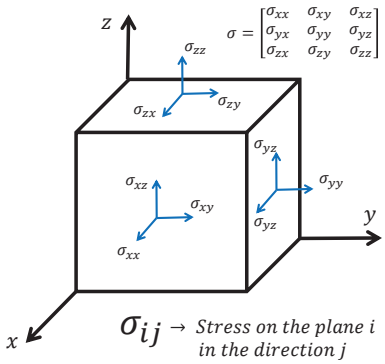

Figure 2: The stress tensor, consisting of nine components.

the material but enables the multi-dimensional nature of stress shown in Fig. 2 to be represented in a single value.

2.1.3. Computational Fluid Dynamics (CFD) and Finite Element Analysis (FEA)

Computational Fluid Dynamics (CFD) and Finite Element Analysis (FEA) are both continuum mechanics methods, which have the goal to represent the behavior of continuous materials. Specifically, CFD is used to simulate fluid flow and FEA is used to simulate solids. Both methods rely on dividing the considered geometry into elements and forming a mesh, which is necessary to solve the complex set of partial differential equations involved.

2.1.4. Autoregressive with Exogenous Terms (ARX) Models

The objective of the ARX modeling strategy is to find appropriate weights ($a_1, a_2, \ldots, a_n$ and $b_1, b_2, \ldots, b_m$) to create a representative model of a dynamic process. The general form of the ARX model is as follows Billings (2013):

$$y(k) = -\sum_{i=1}^{n} a_i y(k-i) + \sum_{j=1}^{m} b_j u(k-j) \tag{2}$$

where $y(k)$ and $u(k)$ represent the discrete time output and input (respectively) at a time step k. In this equation, $y(k)$ represents the output at the current time step. Outputs from the previous n time steps are designated as $y(k-1), y(k-2), \ldots, y(k-n)$ and inputs from the previous m time steps are represented as $u(k-1), u(k-2), \ldots, u(k-m)$. The number of previous outputs n and inputs m considered for the model can be adjusted to increase how well the model represents the data. We define $p = max(n+1, m+1)$.

To find the weights, a set of N data points is used. The data takes the form of a series of values taken at time steps $1, 2, \ldots, N$. The input data can then be represented as $u(1), u(2), u(3), \ldots, u(N)$ and the output data as $y(1), y(2), y(3), \ldots, y(N)$. This data is used to define a vector $Y = [y(p), y(p+1), \ldots, y(N)]^T$ and a matrix X (which is created using the input-output data) and

is defined in the following manner:

$$X = \begin{bmatrix} -y(p-1) & -y(p-2) & \cdots & -y(p-n-1) & u(p-1) & u(p-2) & \cdots & u(p-m-1) \\ -y(p) & -y(p-1) & \cdots & -y(p-n) & u(p) & u(p-1) & \cdots & u(p-m) \\ -y(p+1) & -y(p) & \cdots & -y(p-n+1) & u(p+1) & u(p) & \cdots & u(p-m+1) \\ \vdots & \vdots & \cdots & \vdots & \vdots & \vdots & \cdots & \vdots \\ -y(N-2) & -y(N-3) & \cdots & -y(N-n-2) & u(N-2) & u(N-3) & \cdots & u(N-m-2) \\ -y(N-1) & -y(N-2) & \cdots & -y(N-n-1) & u(N-1) & u(N-2) & \cdots & u(N-m-1) \end{bmatrix}$$

X and Y are then used to solve for a vector of the weights $\theta = [a_1, a_2, \ldots, a_n, b_1, b_2, \ldots, b_m]^T$ as follows:

$$\theta = \left(X^T X\right)^{-1} X^T Y \tag{3}$$

After θ has been determined with one set of data, several other data sets of input-output data (from the same process) should be used to verify the model.

2.2. CFD/FEA Simulation Methods

2.2.1. Fluid Mechanics Simulation

A fully three-dimensional one meter long segment of a single steam methane reforming tube was simulated using ANSYS simulation software v20.1 and is based on the work done in Lao et al. (2016). The gaseous fluid phase flowing through the pipe consists of CH_4, CO, CO_2, H_2O, and H_2, and was simulated using the ANSYS Fluent application. The simulation incorporates Fluent user-defined functions (UDFs) to include custom functionality including the reaction mechanism from Xu and Froment (1989) and an adjustable temperature profile along the outer tube wall (the wall temperature can be adjusted to impact the H_2 concentration at the outlet). The resulting Fluent simulation was coupled with an ANSYS structural simulation to analyze the impacts of temperature and pressure on stress of the tube wall material.

The Fluent simulation assumes viscous flow and the standard $k - \epsilon$ flow model with enhanced wall treatment, which is needed to represent the turbulent flow in the process. This flow model accounts for the complex flow iterations that occur near a solid wall during turbulent flow by including transport equations for the kinetic energy (k) and the rate of dissipation of the kinetic energy (ϵ) to the fluid mechanics simulation. The enhanced wall treatment option creates a layered model near the wall to more accurately represent experimental observations during the simulation of

turbulent flow. These layers consist of a viscous sublayer nearest the wall where the flow is laminar (with a linear velocity profile), a buffer region between the laminar and turbulent flow regions, and fully-turbulent outer region where the flow is logarithmic. Pressure gradient, full buoyancy effects, thermal, and viscous heating effects are active and modify aspects of the $k-\epsilon$ equations to account for the associated phenomena ANSYS (2020a).

The pressure-based solver was used instead of the density-based solver as in Lao et al. (2016). In addition, the porous zone formulation is used to simulate flow through the catalyst Lao et al. (2016). The physical velocity formulation was selected over the superficial velocity formulation because it allows for a prediction of velocity, thus leading to a more accurate model. The porous zone approximation estimates the effects of porous media on the flow by introducing terms that act as a momentum sink through the use of empirically derived parameters ANSYS (2020b). The selected parameters include a viscous resistance inverse absolute permability of 8,782,800 $1/m^2$ and an inertial resistance of 1,782 $1/m$. The fluid porosity was set to be 0.609 Lao et al. (2016).

The density of the gaseous reaction mixture is assumed to be ideal, the specific heat is determined using a mixing law, the ideal-gas mixing laws are assumed to determine the thermal conductivity and viscosity, and kinetic theory is used for determination of mass diffusivity and the thermal diffusion coefficient. The diffusion of material was accounted for by enabling the diffusion energy source, full multi-component diffusion, and thermal diffusion options. The process-side inlet conditions are identical to those in Lao et al. (2016) and include a gauge pressure of 3038.5 kPa, a temperature of 887 K, and a flow rate of 0.1161 kg/s. Inlet mole fractions for each entering species are as follows: 0.2487 for CH_4, 0.0001 for CO, 0.0117 for CO_2, 0.7377 for H_2O, and 0.0018 for H_2. The outlet conditions were given reasonable values from Latham et al. (2011) including a gauge pressure of 2804.0 kPa, and mole fractions of 0.0526 for CH_4, 0.0845 for CO, 0.0575 for CO_2, and 0.4631 for H_2, with the remainder being H_2O. The catalyst material was given a density of 3960 kg/m^3, a specific heat of 880 J/kg-K and a thermal conductivity of 33 W/m-K Lao et al. (2016). The tube wall was assumed to be HP-grade stainless steel, which is a material that has been used for SMR reactors Webb and Taylor (2007). The thermal properties of the tube wall include a density of 7861.10 kg/m^3, a specific heat of 460.18 J/kg-K, and a thermal conductivity of 29.40 W/m-K Steel

Founders' Society of America (2004). Tables 1-2 summarize simulation parameters for reference.

Table 1: Specified conditions for the inlet boundary conditions (identical to Lao et al. (2016)) and a guess for the outlet conditions (from Latham et al. (2011)) for the SMR simulation.

	Inlet Conditions	Outlet Conditions (Initial Guess)
Temperature (K)	887	1143.15
Gauge Pressure (kPa)	3038.5	2804.0
Flow Rate (kg/s)	0.1161	0.1161
CH_4 Mole Fraction	0.2487	0.0526
CO Mole Fraction	0.0001	0.0845
CO_2 Mole Fraction	0.0117	0.0575
H_2O Mole Fraction	0.7377	0.3423
H_2 Mole Fraction	0.0018	0.4631

Table 2: Simulation parameters: Catalyst and fluid phase properties (taken from Lao et al. (2016)), tube wall HP-grade stainless steel material properties (Steel Founders' Society of America (2004)), empirically derived porous phase parameters (ANSYS (2020b)), and dimensions of geometry (radii are the same as in Lao et al. (2016)).

Catalyst Density	3960 kg/m^3
Catalyst Specific Heat	880 J/kg-K
Catalyst Thermal Conductivity	33 W/m-K
Fluid Phase Porosity	0.609
Wall Density	7861.10 kg/m^3
Wall Specific Heat	460.18 J/kg-K
Wall Thermal Conductivity	29.40 W/m-K
Wall Young's Modulus	2.7×10^7 psi
Wall Poisson's Ratio	0.3
Wall Thermal Expansion	1.312×10^{-5} 1/F
Viscous Resistance (Inverse Absolute Permability)	8,782,800 1/m^2
Inertial Resistance	1,782 1/m
Tube Length	1 m
Tube Outer Radius	0.073 m
Tube Inner Radius	0.063 m

The furnace-side reaction was not simulated. Instead, the following equation from Lao et al. (2016) was applied along the outer tube wall via a UDF:

$$T(z) = -0.0221z^4 + 0.8003z^3 - 10.734z^2 + 64.416z + (T_{wall}^{max} - 151.83) \tag{4}$$

where z represents the length coordinate along the pipe length and T_{wall}^{max} represents the highest temperature applied by the heat source in Kelvin. As in Lao et al. (2016), a UDF is used to

modify the value of T_{wall}^{max}. Finally, under-relaxation factors of 0.3 (which are used in the pressure-based solver for controlling how variables are updated at each iteration ANSYS (2020b)), double precision, a coupled pressure-velocity formulation, and second order upwind spatial discretization were utilized.

Remark 1. *The reforming tube model is only a 1 m segment of what was a longer (12.5 m) tube in Lao et al. (2016). In addition, the reforming tube model is a simplified model, as reflected by the fact that it includes a heat profile along the wall that is being adjusted by the control strategy. In a full reformer, the temperatures along the walls of the reforming tubes are not adjusted explicitly, but instead the flow rates of fuel through burners can be adjusted. The geometry can create temperature profiles on the outer tube walls that are not the same for all reforming tubes in a full reformer Tran et al. (2017b). The direct control of the temperature of the tube wall will affect the results for the stress on the walls, as it enables sudden jumps in the temperature at the walls which would not be possible in a physical system due to the need to change the temperature of the tube walls through first manipulating the burner flow rates. These differences between a physical system and the simulated system do not, however, detract from the main message of this section, which is that CFD and FEA analysis provides a useful modeling framework for analyzing impacts of dynamic operating policies on equipment, either directly in the software or through using the software to develop reduced-order models that can then be used for modeling the impacts of the dynamic operating policies on equipment in software such as MATLAB or Ipopt.*

2.2.2. Structural Simulation

The results of the fluid flow simulation were imported into ANSYS Transient Structural to perform a transient solid mechanics simulation. This includes the temperature profile in the solid and the pressure profile along the inner surface of the tube. This form of coupling Fluent to Transient Structural is one-directional, as the entire Fluent simulation is completed before starting the structural simulation. This reflects the assumption that the deformation of the solid does not have an impact on the fluid flow simulation, which is reasonable as the deformation of the pipe would be expected to remain relatively small. It is also assumed that the pipe material remains entirely in the elastic region.

In the Transient Structural simulation, one end of the tube was set to have a fixed boundary condition, which prevents displacements in all directions. In addition, atmospheric pressure of 101,325 Pa was applied along the outer surface of the tube, and a gravitational force was included. The direction of gravity was set to be in the same direction as the fluid flow, as the SMR reactor being simulated is top-fired. The ambient temperature is assumed to be at room temperature. Finally, the HP steel tube wall was assigned a value of Young's Modulus of 2.7×10^7 psi, a Poisson's Ratio value of 0.3, and a thermal expansion coefficient of 1.312×10^{-5} 1/F Steel Founders' Society of America (2004). In addition, to consider only elastic deformation, the yield and ultimate strengths were set to arbitrarily high values of 1×10^{30} Pa.

2.3. Considerations Regarding CFD/FEA Simulation Consistency and Precision

2.3.1. Simulation Convergence

Given that both the Fluent and Transient Structural simulations are iterative calculations, it is important to ensure that the results converge to a value after a sufficient number of iterations have been completed. In this paper, convergence of the Fluent simulations was ensured by monitoring the residuals and heat flux balance during the simulation.

Fluent residuals are values that are calculated at the end of each iteration and consist of a weighted sum of the conservation of each variable across all elements in the mesh. As the simulation approaches convergence, the residuals approach zero ANSYS (2020b). For simulations completed in this work, the residuals were ran until they leveled off and were on the order of magnitude of, at most, 10^{-7}.

The heat flux balance is a scalar value that represents the sum of energy (in Joules) entering and leaving the overall system. For steady-state simulations, the total heat flux should approach a value of zero. This may not be true for the transient simulations where the system is no longer at equilibrium. For simulations completed in this work, it was ensured that the total heat flux values fell below an order of at least 10^{-3} W for the steady-state simulations and leveled off between each time step of a transient simulation.

Table 3: Meshes used for mesh independence testing (1m tube).

Elements in r direction*	Elements in θ direction	Elements in z direction	Number of Fluid Elements	Number of Solid Elements
7	52	125	101,184	41,664
10	72	180	222,139	121,720
14	100	250	478,080	334,656
23	168	411	1,630,570	1,546,520

*In the solid

2.3.2. Mesh Independence

The method of solving both CFD and FEA problems involves discretizing the domain into a grid called a mesh. The mesh consists of discrete points called nodes, which are connected together to form elements. In general, smaller elements will lead to a more accurate CFD result; however, computation time becomes a limiting factor. Therefore, it is necessary to select a mesh that balances computation time and solution accuracy. To do this, a mesh independence test is applied that involves repeatedly solving the problem with progressively finer meshes and comparing results, such as temperature or stress. The mesh was considered to be sufficiently fine when the change in results between a coarser and finer mesh was within a certain threshold. In this study, ANSYS ICEM CFD was used to generate geometry and meshes.

In the meshes used in this test, the ratio of the dimensions of the elements in the solid was maintained when decreasing the element size. The selected ratio of 14:100:250 was approximately enforced (rounding when needed), which represents the number of elements in the r, θ, and z directions respectively. This was accomplished through changing the number of divisions in the mesh along the edges of the geometry. This also fixes the number of elements in the fluid, as both the fluid and solid meshes are created simultaneously. The number of divisions in the r direction in the fluid is set at 15 and remains constant for all meshes tested. The number of elements applied in the meshes for the fluid and solid domain are displayed in Table 3.

Figure 4 plots the equivalent stress for four different meshes following the inputs given in Figure 3. These meshes are identified by the number of divisions in the r direction (r=7, r=10, r=14, and r=23). The legend also contains other labeling (such as original and simplified, the time step size,

and whether the loads were ramped or stepped), which will be discussed in the following sections. Looking at Figure 4, the largest change occurs when increasing the number of elements from the r=7 to the r=10 mesh. Further refinements to r=14 and r=23 are relatively small. Given this, the r=10 mesh is considered sufficiently independent for the purposes of demonstrating the use of CFD/FEA simulations in analyzing control and equipment interactions in this work and will be used in the final simulations. We note that because no steady-state structural simulation was performed, in all structural simulations in this work, the model is initially run at a steady-state to enable the structural simulations to reach a result that appears to represent an initial equilibrium condition in the plots.

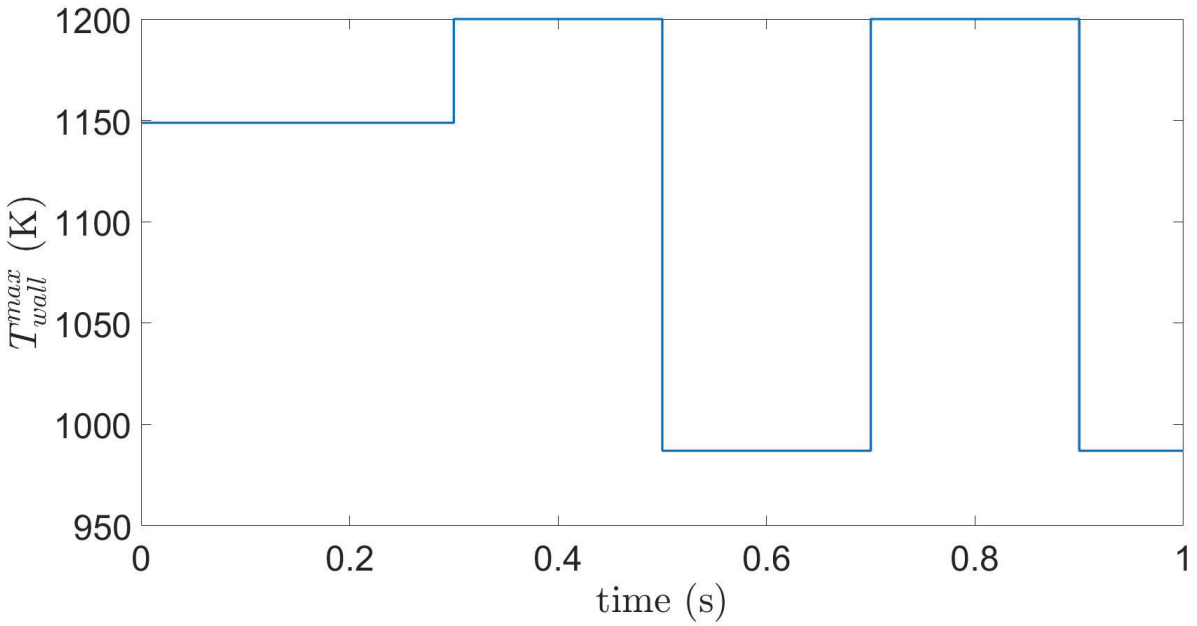

Figure 3: Value of T_{wall}^{max} over time.

2.3.3. Stepped and Ramped Loads

In Transient Structural, it is possible to apply the temperature and pressure loads as either stepped (i.e., the load is fully applied at the beginning of each time step) or ramped (i.e., the load is applied gradually over the course of calculating the results of a time step) when performing the calculation. To ensure that the method selected would not impact the FEA results, we compared the results of these two methods by checking the values determined at the end of each time step. To determine the significance of the difference between stepped and ramped loads, T_{wall}^{max} inputs were

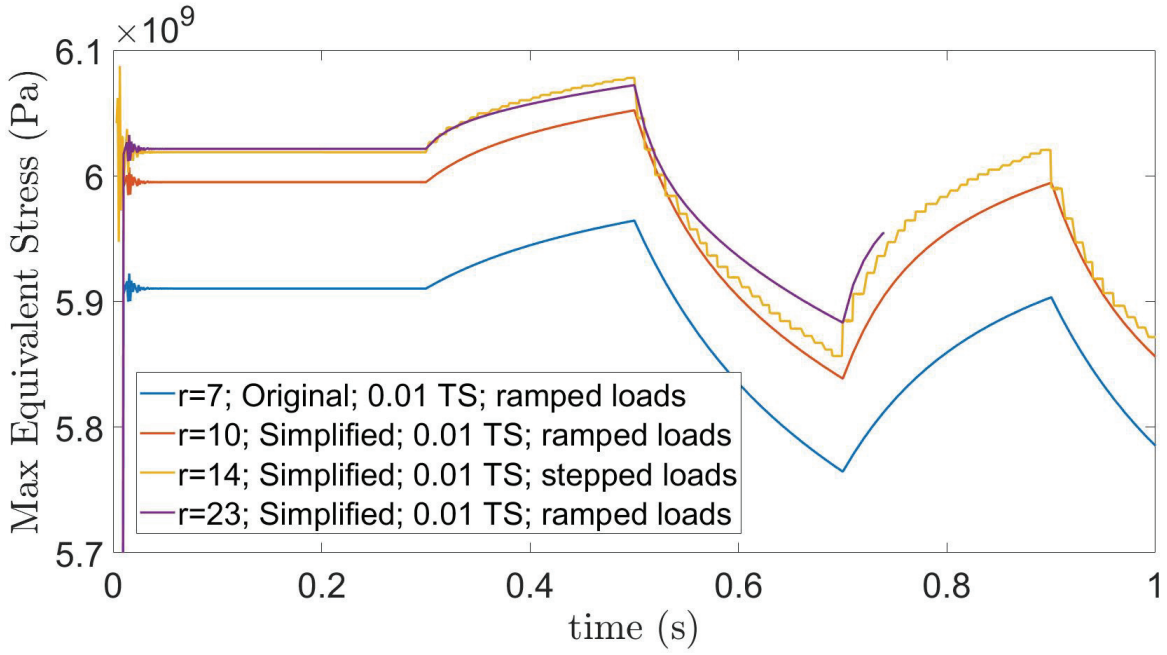

Figure 4: Comparison of structural results based on different meshes.

supplied to the system (Figure 3) and the resulting von Mises stresses were determined (Figure 5). Displayed are the von Mises stress results for the r=7 and r=10 meshes with both ramped and stepped loading. The values in between each time step (the values calculated at each sub time step) vary slightly, but the results are similar. Therefore, in this work, ramped loads will be favored because they give more natural and smooth looking results.

2.3.4. Fluent Simplifications

Through the examination of results of the fluid flow simulation, it was found that several features could be disabled to speed up the simulations without significantly affecting the structural results. To demonstrate this, transient Fluent simulations were created with the following options disabled: pressure and thermal gradient, buoyancy, and viscous heating effects in the $k-\epsilon$ wall model, and the diffusion energy source, full multi-component diffusion, and thermal diffusion options. These changes allow for the under-relaxation factors to be increased from 0.3 to 0.5 which allows for faster convergence. The results of this analysis are shown in Figure 6, in which the same set of inputs were applied as in previous sections (Figure 3). The simplified Fluent simulation results do not meaningfully change the transient structural equivalent stress results for both the r=7 and r=10 meshes. Therefore, the final simulations will use the simplified setup.

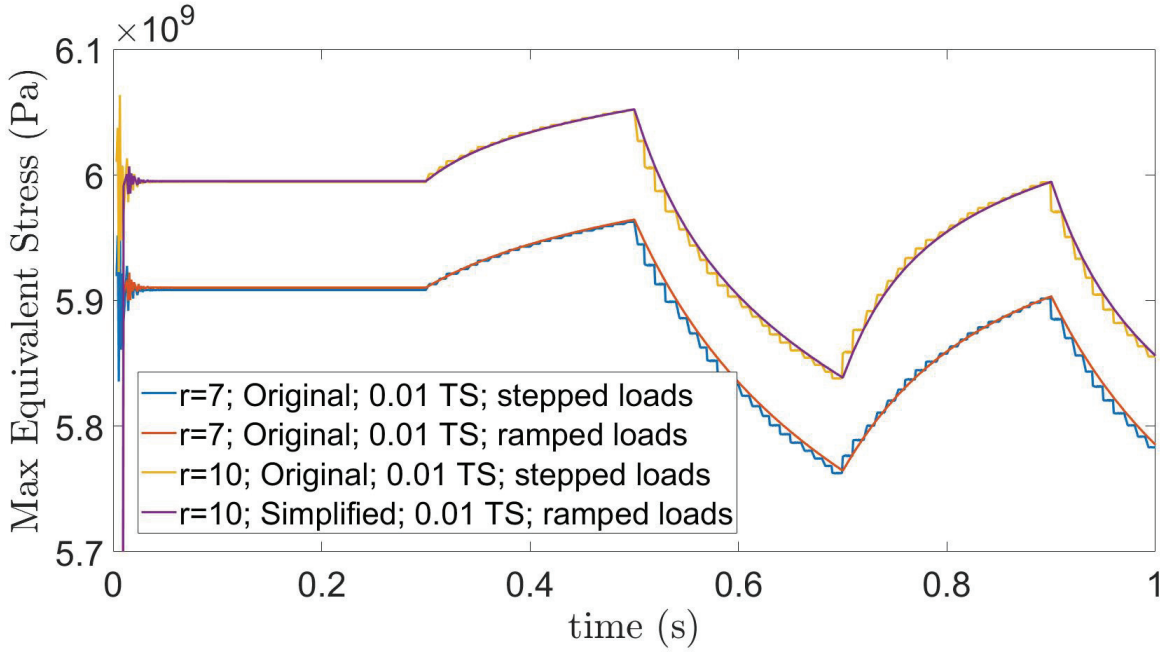

Figure 5: Comparison of maximum equivalent stress when structural loads (temperatures and pressures) are applied in a stepped and ramped manner.

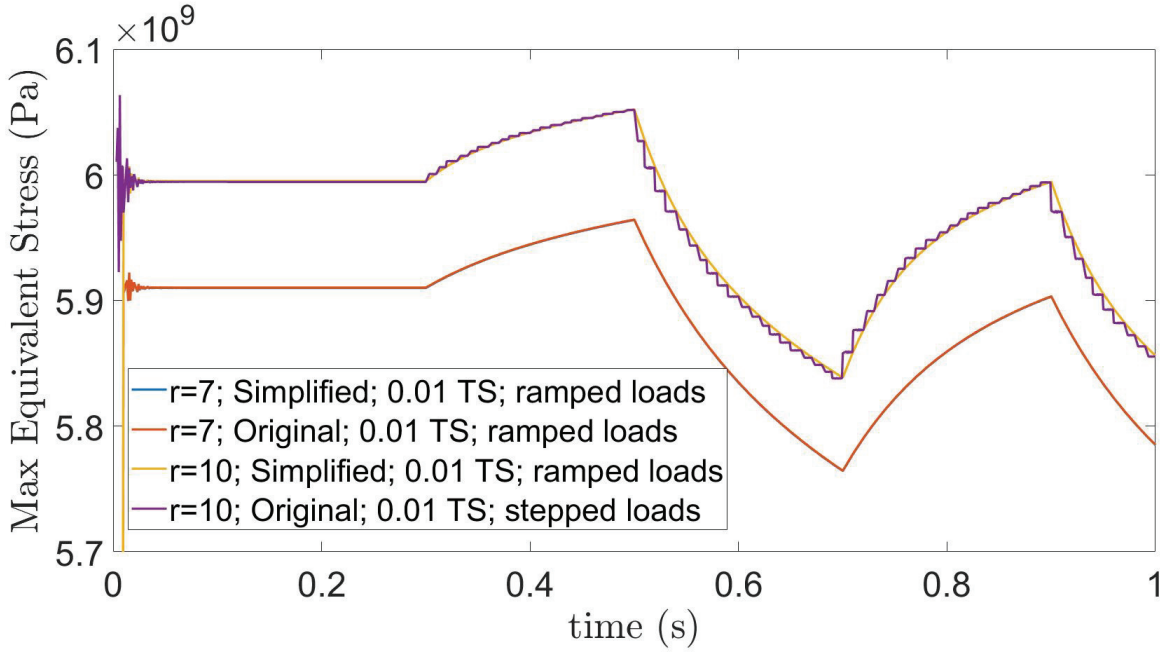

Figure 6: Comparison of structural results based on imported loads from the original Fluent simulation (with all options enabled) compared to imported loads from a simplified Fluent simulation.

2.3.5. Time Step Independence

Another consideration is the need for the simulation results to be independent of time step size. In general, smaller time steps will lead to more accurate results. However, this also increases

computation time. Therefore, a series of simulations was completed with progressively smaller time steps and the results are compared. The results should converge to a solution that is independent of the time step, and the largest of the converged time steps should be selected. In this study, four different time step sizes were simulated with the r=10 mesh. These include time steps of 0.005 seconds, 0.05 seconds, 0.01 seconds, and 0.02 seconds. The results of this analysis are shown in Figure 7, in which the same set of inputs were applied as in previous sections (Figure 3). The von Mises stress results demonstrate that decreasing the time step size below 0.01 seconds creates a relatively small difference in the maximum equivalent stress. The final simulations will thus use this time step size.

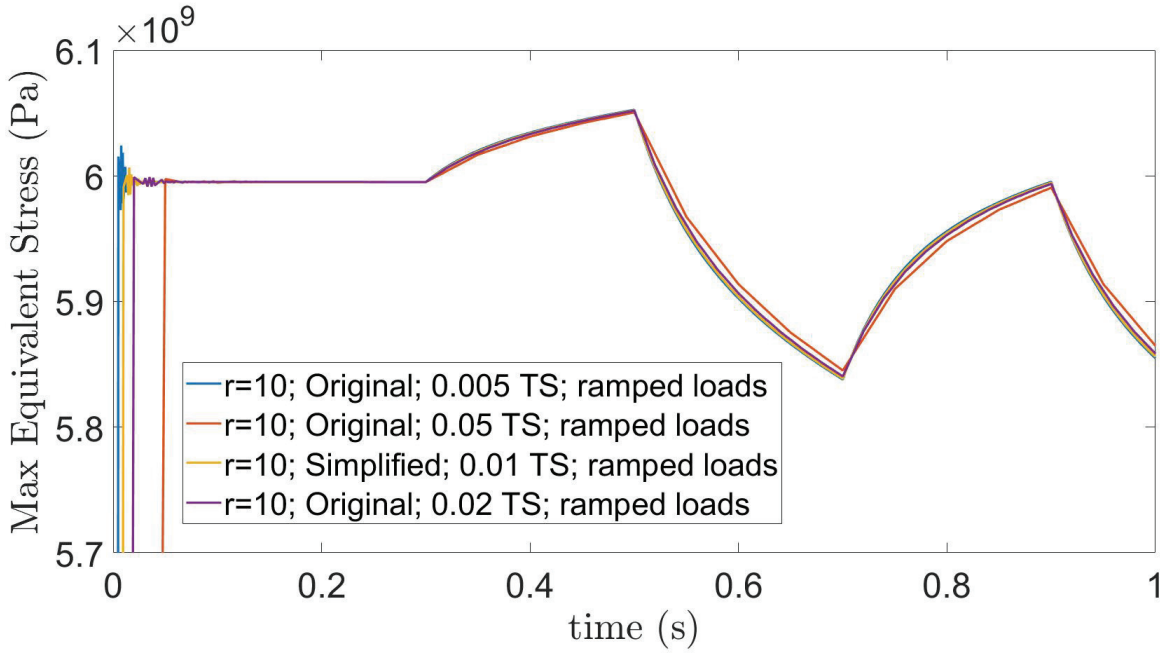

Figure 7: Comparison of structural results based on different time steps.

2.4. Cyberattack Simulation Results

The purpose of this section is to demonstrate the use of coupled CFD/FEA simulations in analyzing equipment response to a cyberattack on the actuator of the steam methane reforming tube described in sections 2.2.1 and 2.2.2 with the $r = 10$ mesh. In these simulations, the value of T_{wall}^{max} was set to certain values to represent a cyberattack that targets the sensor measurements. In the first simulation (see figures 8 and 9), the simulation begins at a steady-state of $T_{wall}^{max} = 987$ K. After a short period of time, a cyberattack is applied where T_{wall}^{max} is set to 1050 K. This causes

both the area-weighted hydrogen mole fraction at the outlet and the maximum equivalent stress to increase. The second attack (see figures 10 and 11) represent a more complicated attack. Here, after a steady-state period at $T_{wall}^{max} = 1148.83$ K, the value of T_{wall}^{max} is attacked to cycle from the upper and lower bounds on T_{wall}^{max} every 0.2 seconds. The outlet hydrogen mole fraction remains relatively steady, but begins to decrease after about a second. The maximum equivalent stress, however, increases and decreases rapidly along with the temperature changes (the time axis in Fig. 11 is shorter than that in Fig. 10).

In the second simulation where the value of T_{wall}^{max} oscillates (figures 10 and 11), it is worth noting that the outlet hydrogen mole fraction decreases because the attack is unbalanced around the initial steady-state. That is, the distance T_{wall}^{max} falls is greater than the distance when it increases. If T_{wall}^{max} oscillated evenly around the steady-state (for example, by repeatedly increasing and decreasing by 100 K), the hydrogen mole fraction would be expected to change negligibly. This means that a hydrogen concentration sensor at the outlet would not be able to detect the attack, but the tube wall would experience significantly more stress. This demonstrates how simulation can reveal consequences of cyberattacks. In this case, adding another sensor (such as a temperature sensor to detect the tube wall temperature, or a flow rate sensor to detect the change in combustion feed) would help ensure this attack could be detected.

These simulations could be modified to represent a wide variety of attacks if desired and indicate that a potential utility of CFD/FEA could be in evaluating safety hazards due to control system cyberattacks while also exploring the impacts of attacks on, for example, profitability. Though this example considers a relatively small system (a portion of a single tube), CFD/FEA simulation of systems under control system cyberattacks has the potential to be helpful in cases where outcomes of those problems are more complex or difficult to predict.

2.5. Other Dynamic Operating Policies: Advanced Control Simulation Results

This section discusses how CFD/FEA simulations might be used to analyze relationships between control and equipment. Here, we first use the CFD/FEA simulations to develop reduced-order models of the SMR process. Two linear single-input-single-output models were made using the autoregressive with exogenous terms (ARX) model to relate T_{wall}^{max} to (1) the outlet hydrogen mole

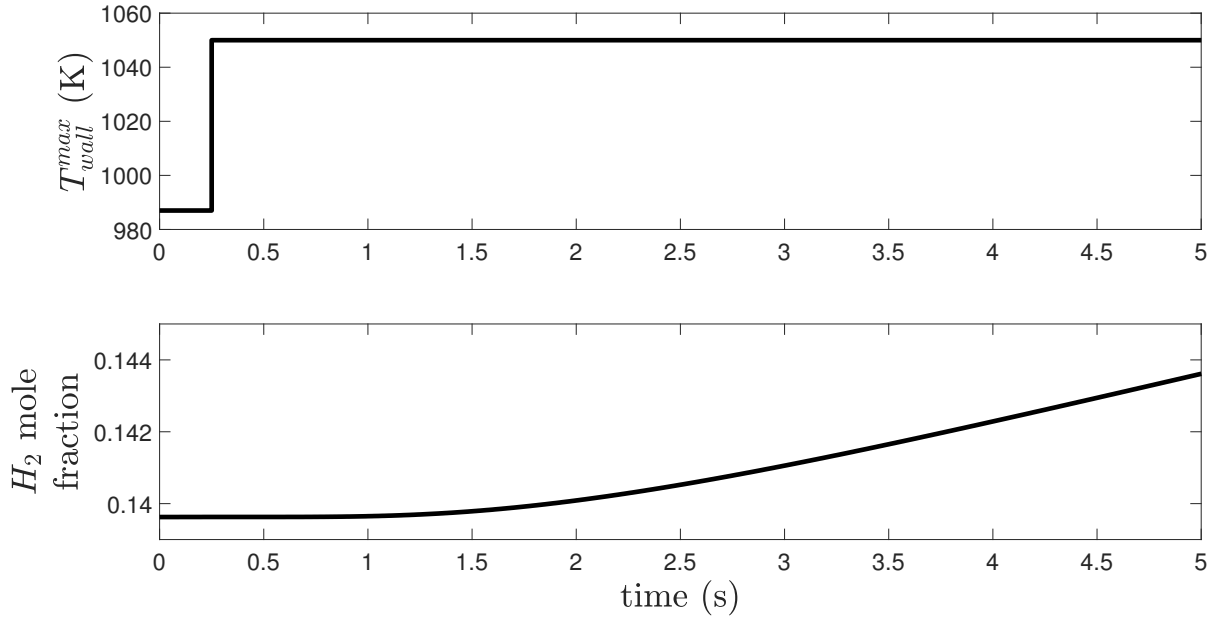

Figure 8: Top: T_{wall}^{max} attack profile for a stepped attack. Bottom: Resulting area-weighted H_2 mole fraction at the outlet of the 1 m tube.

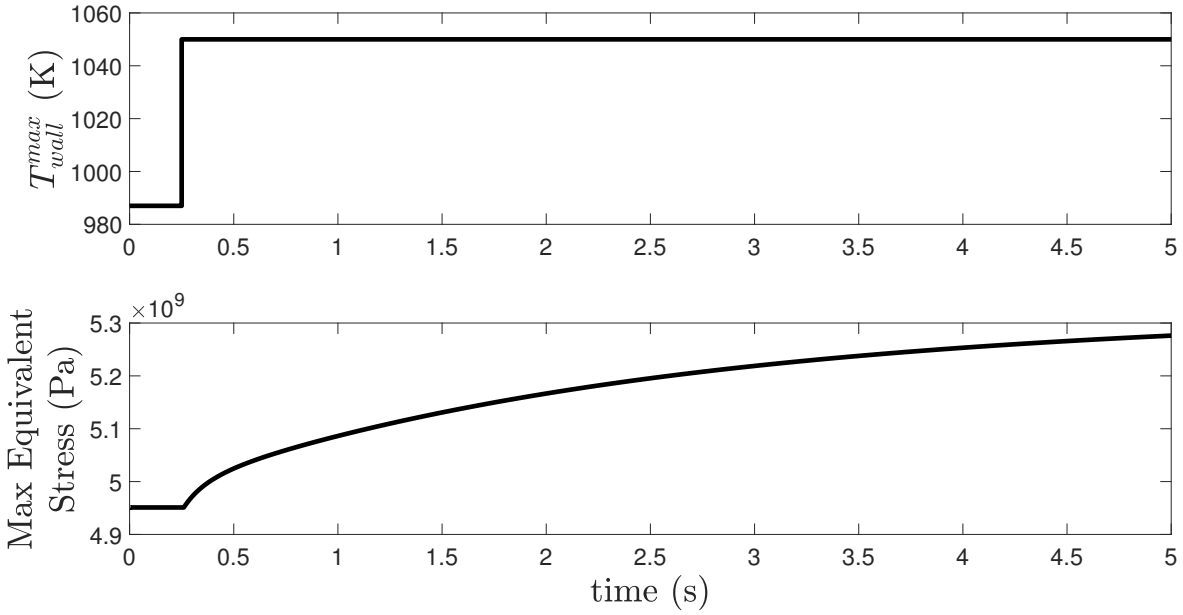

Figure 9: Top: T_{wall}^{max} attack profile for a stepped attack. Bottom: Resulting maximum equivalent stress.

fraction and (2) the maximum overall value of equivalent stress in the tube. Then we develop several model predictive control (MPC) simulations with different constraints. The first MPC maximizes the hydrogen outlet concentration without knowledge of the impacts on equivalent stress for

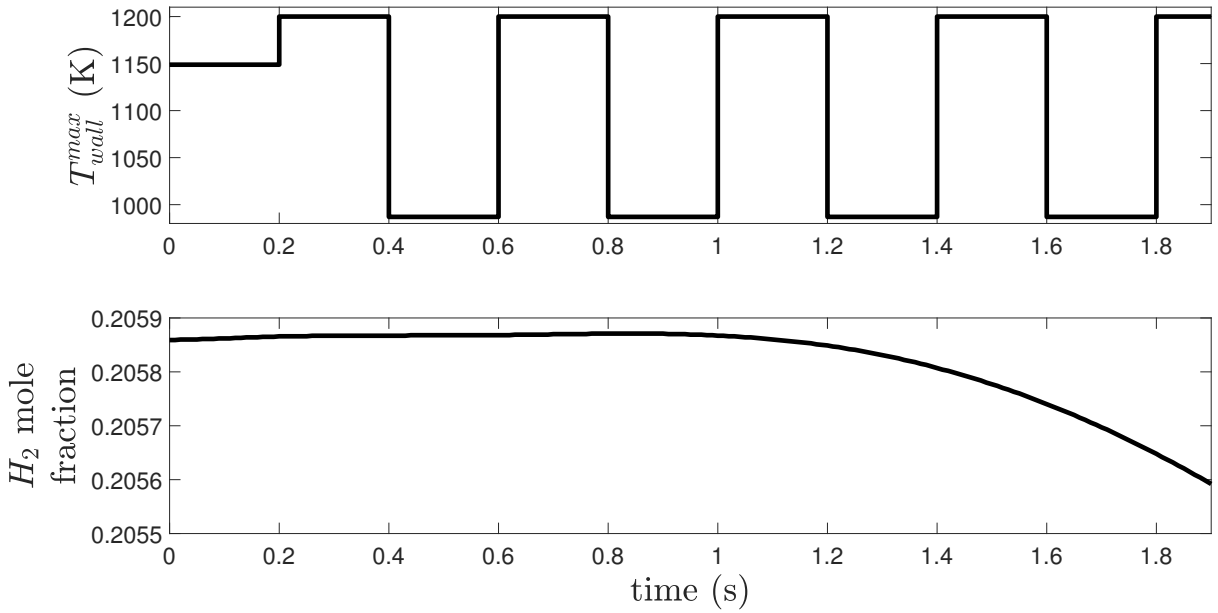

Figure 10: Top: T_{wall}^{max} attack profile for an oscillating attack. Bottom: Resulting area-weighted H_2 mole fraction at the outlet of the 1 m tube.

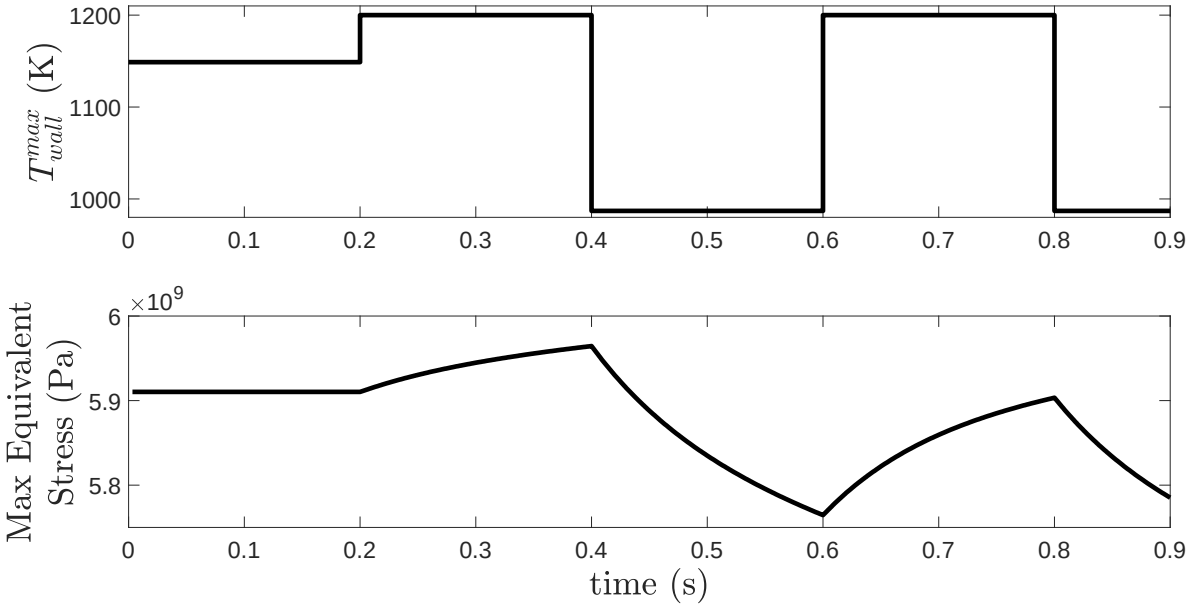

Figure 11: Top: T_{wall}^{max} attack profile for an oscillating attack. Bottom: Resulting maximum equivalent stress.

a given initial condition. The second controller optimizes the hydrogen mole fraction and contains a constraint to constrain the von Mises stress to be below a specified value. The third MPC applies a material constraint which is designed to ensure that the average feed fuel rate is maintained at a

specified value while optimizing hydrogen outlet concentration (more details are included below). Finally, the fourth MPC applies both the equivalent stress and material constraints. In all cases, the hydrogen mole fraction ARX model is used in the objective function for computing control actions. Here, we explore the possibility that reduced-order models of hydrogen concentration and stress developed from the CFD/FEA simulation data may provide a means for quickly postulating effects of different control cyberattacks on equipment fidelity as well as process profitability.

2.5.1. Outlet Hydrogen Mole Fraction Model

In Fig. 7, a time step size for solving the coupled Fluent/Structural simulation was selected based on time independence studies. The same time step size was used for both the CFD and FEA studies in that case due to the manner in which the Structural results depend on the Fluent results. However, the timescale at which the transport phenomena evolve in Fluent is slower than that in the structural studies. Therefore, for developing the reduced-order model, we will explore using larger time steps in the ARX model for the outlet hydrogen mole fraction compared to the time step that would be needed for the ARX model for the maximum equivalent stress. To ascertain the step size to use for the outlet hydrogen mole fraction, three different open-loop input trajectories were utilized that had similar aggregate characteristics (the top figure in Fig. 12). Specifically, for all three trajectories, three average values of T_{wall}^{max} were achieved, but with added noise consisting of a randomly-selected value of ± 10 K added to the input trajectory at every time step (because the time steps were different, this caused different trajectories of the inputs around the three different average temperatures). The goal of including both larger-scale and smaller-scale variations in the inputs when comparing the hydrogen mole fraction results with different time steps was to explore to what extent the various types of changes impacted the hydrogen mole fraction profiles. As shown in Fig. 12, when three time steps of 0.01, 0.05, and 0.1 seconds were used, the results over 8 seconds of simulation were similar with both types of changes to the inputs. Due to this, we considered that the step size of 0.1 seconds was adequate compared to the 0.01 and 0.05 second time steps. To investigate whether the time step size for the outlet hydrogen mole fraction model could be further increased, another simulation with aggregate and small-scale variations in T_{wall}^{max} was used to compare time steps of 0.1 seconds and 0.5 seconds (see figure 13). Because this second comparison

was between two models with longer time steps, it could be used to analyze a longer time period of operation (in this case, variations in the inputs occurred for over 35 s) without the computational challenge of simulating the 0.01 and 0.05 second models over such a long time period. Again the difference between the outlet hydrogen mole fraction trajectories appeared to be small over the time period simulated, so that the time step of 0.5 seconds was selected for the hydrogen mole fraction ARX model and for generating data specifically for identifying this model. Based on Fig. 7, the time step of 0.01 seconds continued to be used for the equivalent stress ARX model and for the data sets used in identifying it.

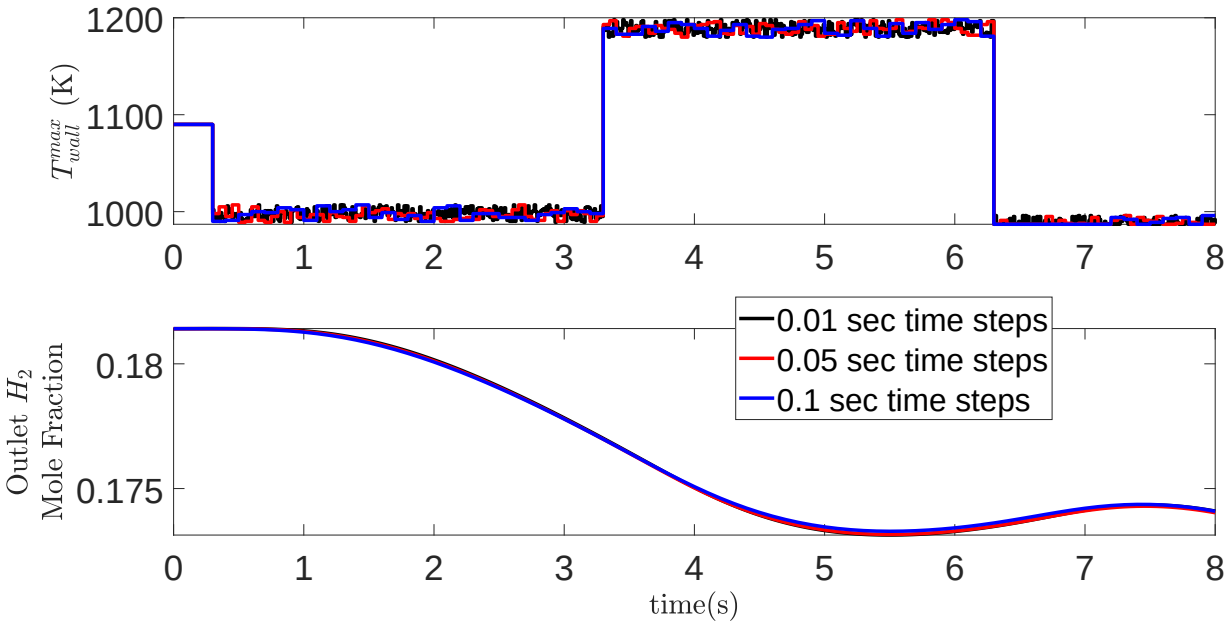

Figure 12: Top: Open-loop input T_{wall}^{max} data for three different simulated time steps (0.01, 0.05, and 0.1 seconds). Bottom: The resulting outlet H_2 mole fraction profiles.

The outlet hydrogen mole fraction ARX model was developed using the simulation shown in figure 14 and validated using four other sets of data (two of which are shown in figures 15 and 16). All of these sets of data were created using simulations with 0.5 second time steps. These simulations consist of ANSYS Fluent simulations that were run in an open-loop manner with different sets of inputs. ARX models were created with 5 through 11 terms, and the resulting mean errors were determined using the following equation, which is the square root of the average of the sum of

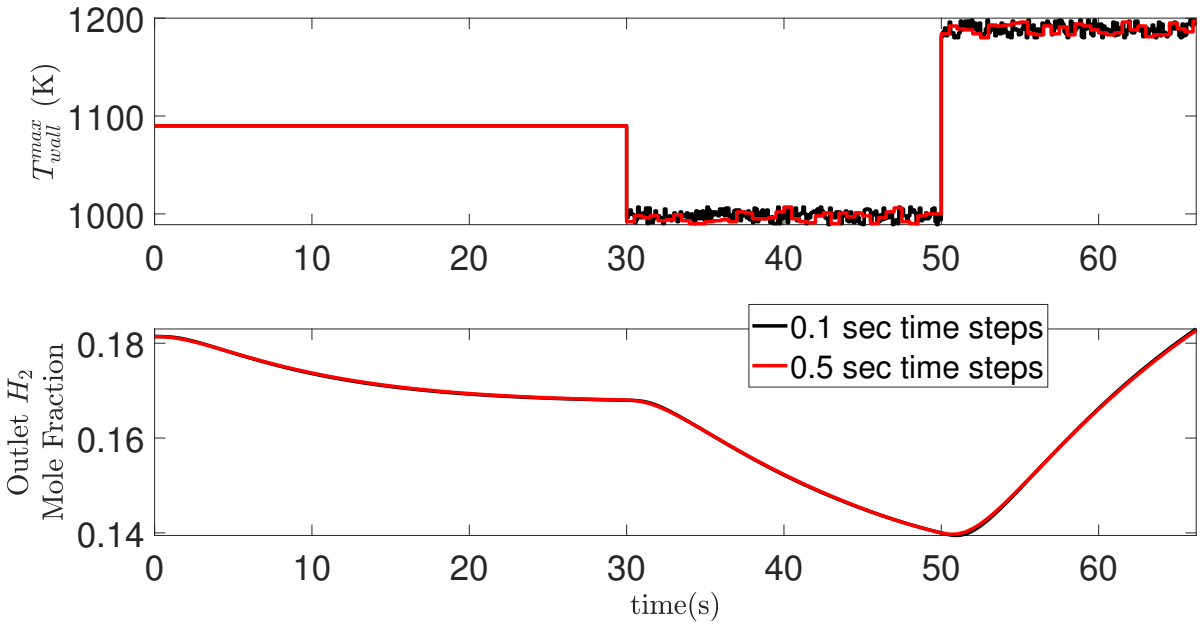

Figure 13: Top: Open-loop input T_{wall}^{max} data for two different simulated time steps (0.1 and 0.5 seconds). Bottom: The resulting outlet H_2 mole fraction profiles.

squared deviations Rhinehart (2016):

$$Error = \sqrt{\frac{\sum_{i=1}^{N}(y_i - \tilde{y}_i)^2}{N}} \tag{5}$$

where N is the number of data points, y_i is the i-th data point from the CFD/FEA simulation results, and $\tilde{y}_i$ is the i-th value from the fitted ARX model.

Based on these metrics, the simplest model (i.e., the model with the fewest input and output terms) with small error values for the considered validation data was selected. The error values tend to decrease as the number of terms increases from 5 to 9, but some of the error values increased substantially when increasing the number of terms to 10 or 11. In addition, it was also ensured that the error is several orders of magnitude lower than the data itself. Based on these results, the an ARX model with 9 terms was selected.

2.5.2. Equivalent Stress Model

The selection of the maximum equivalent (von-Mises) stress model followed a similar procedure as the outlet hydrogen mole fraction model. This time, models with 1 through 6 terms were created. The error values decrease significantly going from the 1 to 3-term models, and then they decrease

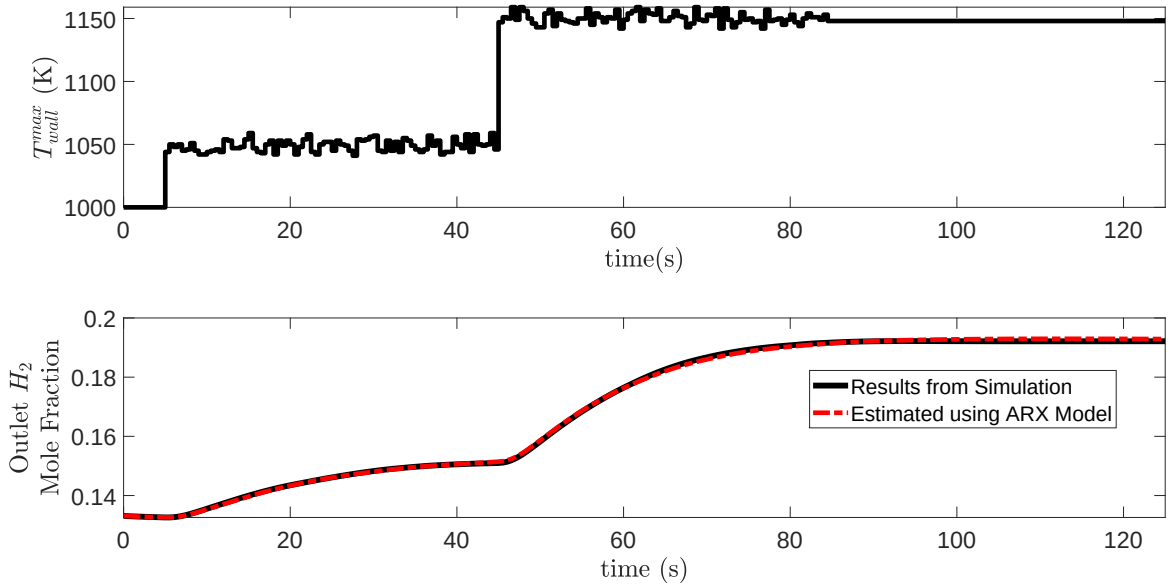

Figure 14: Data set used for fitting the outlet H_2 mole fraction ARX model.

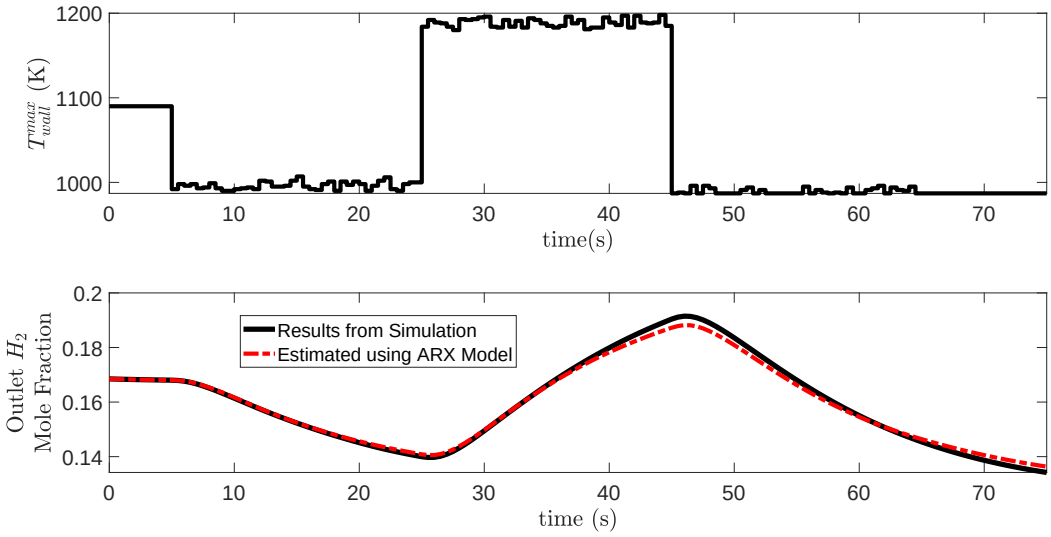

Figure 15: A set of data used to validate the outlet H_2 mole fraction ARX model.

more gradually for 4 or more terms. Given this, a 4-term model was selected. The data set used to determine the paramteters for the ARX model is shown in figure 17, and two sets of validation data are shown in figures 18 and 19.

Remark 2. *These studies used only a limited amount of data to develop the ARX models for the reformer and the equipment due to the computation time needed for solving the CFD/FEA system*

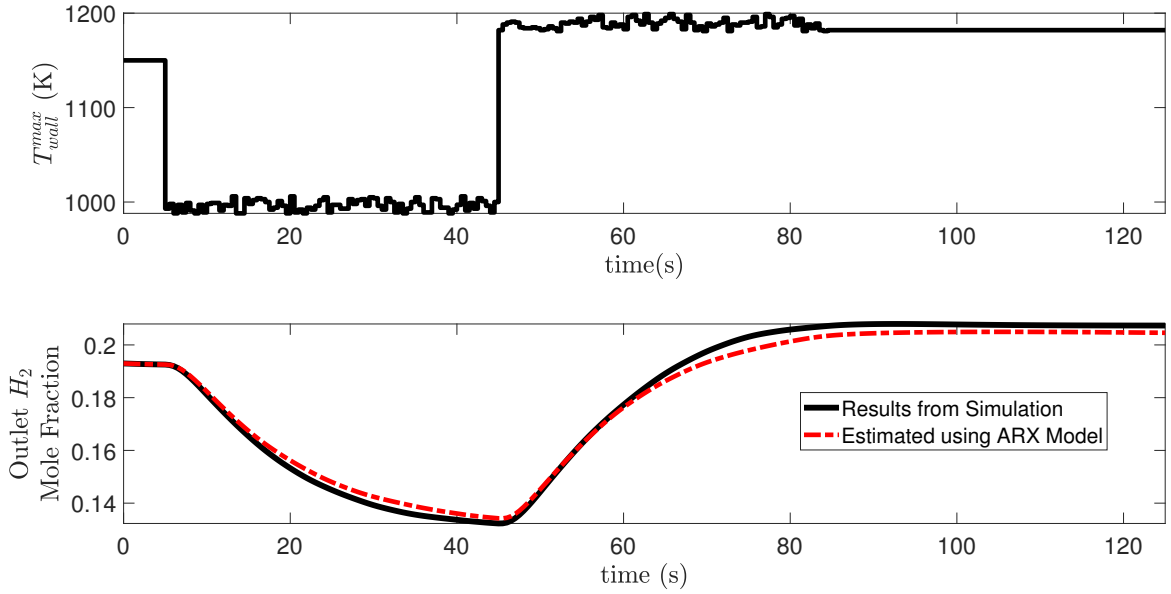

Figure 16: A set of data used to validate the outlet H_2 mole fraction ARX model.

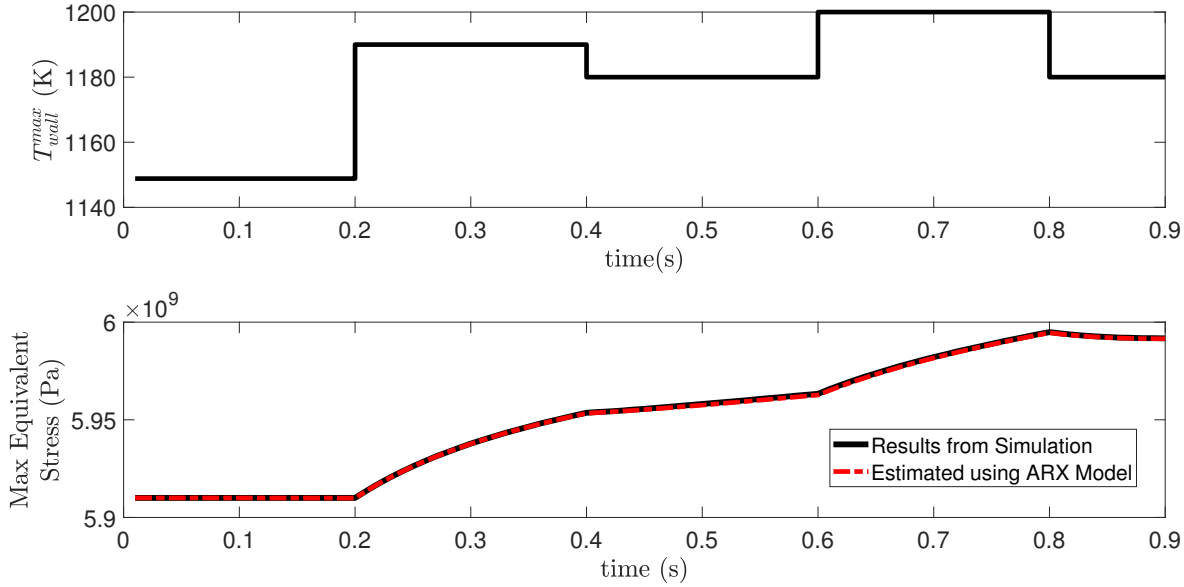

Figure 17: Data set used for fitting the maximum equivalent stress ARX model.

and the fact that the models obtained provided results that were in line with what was expected when used in the model predictive controllers described in the following sections. If CFD or FEA modeling was to be used in industry for analyzing impacts of equipment stress, a more thorough benchmarking strategy may be used, with additional data, to fully validate the models, and other model structures

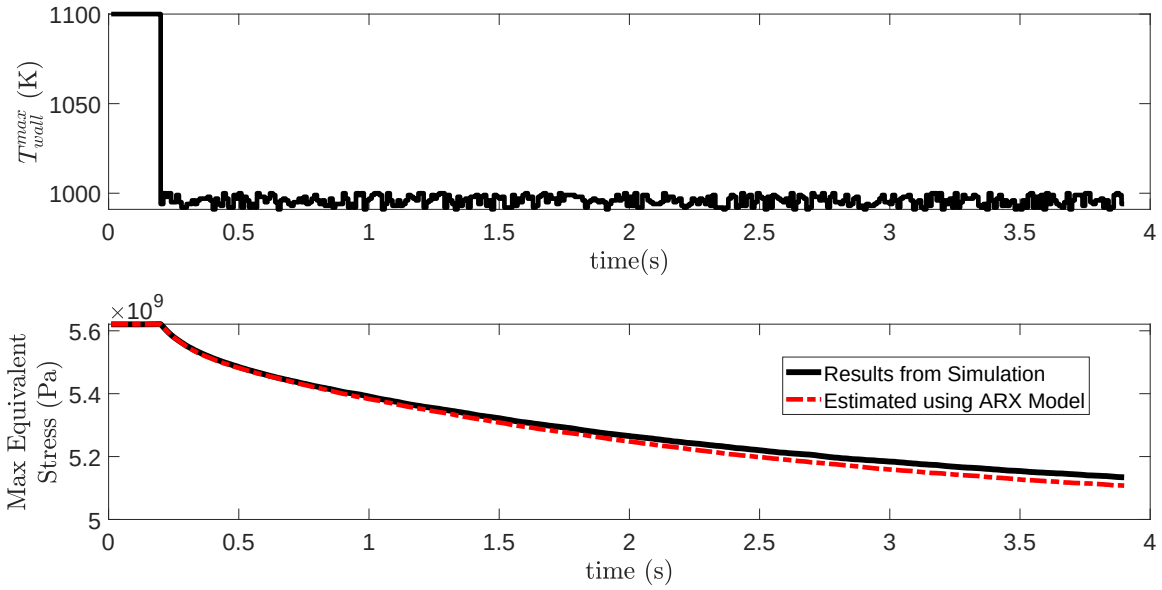

Figure 18: A set of data used to validate the maximum equivalent stress ARX model.

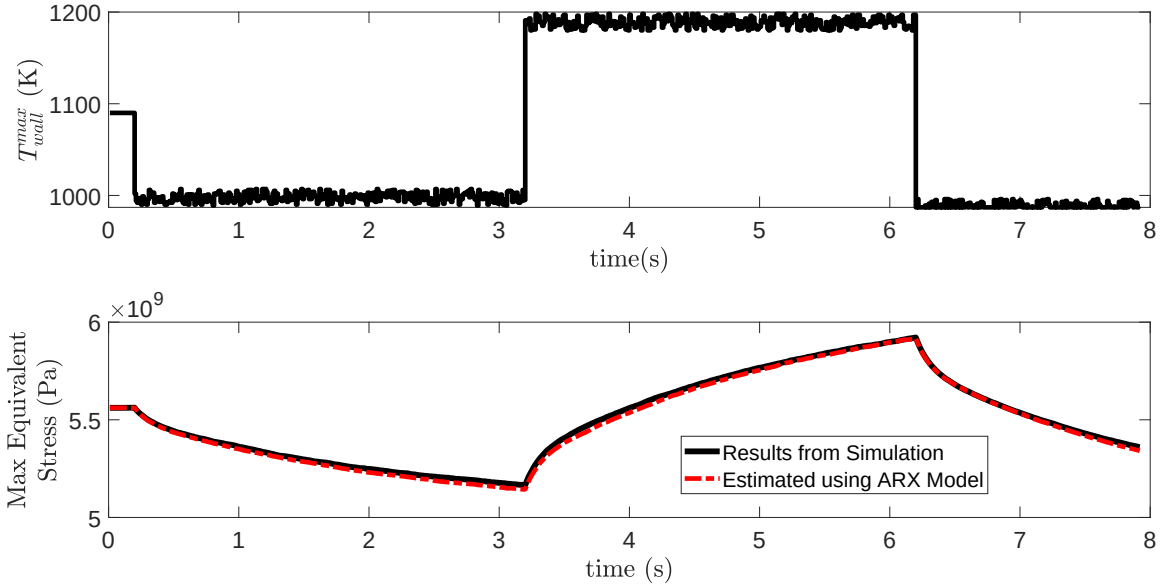

Figure 19: A set of data used to validate the maximum equivalent stress ARX model.

that can capture nonlinearities (e.g., neural networks) might also be considered.

2.5.3. Material Constraints

In order to enforce time-varying operation, a constraint (similar to one applied in Ellis et al. (2014b)) on the material consumption of fuel was included. The purpose of the constraint is to

ensure that the average amount of material used (in this case, fuel supplied by the burner) remains constant. To achieve this, the total time of operation is divided into "operating periods," each consisting of M sampling periods. Within each, the following constraints are applied:

$$MF_{fuel,ave} - \sum_{j=k}^{min(k+N,M-1)} F_{fuel}(\tau_j) - \sum_{i=0}^{k-1} F^*_{fuel}(\tau_j) \leq max(M-N-k,0)F_{fuel,max} \tag{6}$$

$$MF_{fuel,ave} - \sum_{j=k}^{min(k+N,M-1)} F_{fuel}(\tau_j) - \sum_{i=0}^{k-1} F^*_{fuel}(\tau_j) \geq max(M-N-k,0)F_{fuel,min} \tag{7}$$

where M represents the number of sampling periods in an operating period, N represents the number of sampling periods in the prediction horizon (note that $N < M$ is assumed), $F_{fuel,ave}$ is the desired average fuel consumption, $\tau_1, \tau_2, ...$ represents the numbering of the sampling periods within each operating period (the number is set to one at the beginning of each operating period), F_{fuel} represents the fuel usage to be estimated in the prediction horizon by the controller, F^*_{fuel} represents previously determined fuel usages, and the upper and lower allowable fuel usage are $F_{fuel,max}$ and $F_{fuel,min}$ respectively.

The overall idea with these constraints is that $MF_{fuel,ave}$ represents the amount of fuel available in each operating period to ensure that the average fuel usage remains at $F_{fuel,ave}$. During previous sampling periods, the controller applied control actions that consumed an amount of fuel represented by $-\sum_{i=0}^{k-1} F^*_{fuel}(\tau_j)$. In the current prediction horizon and operating period, the controller will select optimal actions that consume an amount of fuel represented by $-\sum_{j=k}^{min(k+N,M-1)} F_{fuel}(\tau_j)$. The sum of these three terms is bounded by the minimum and maximum amount of fuel that could be consumed during the remaining sampling periods in an operating period, represented as $max(M-N-k,0)F_{fuel,min}$ and $max(M-N-k,0)F_{fuel,max}$ respectively. The purpose in implementing the constraints in this way is that it ensures that an average fuel usage is maintained without needing to optimize over the entire time of operation.

For the controller to decide on optimal F_{fuel} values, a relationship was developed between F_{fuel} and T^{max}_{wall}. An overview of this process is included in the following paragraphs.

The energy generated by the burner (E_{flame} in units of energy/time) that supplies heat to the reaction tube can be estimated using the flow rate of fuel to the burner (F_{fuel} in units of moles/time), the heat of combustion (ΔH_{comb} in units of energy/mol), and an efficiency (η):

$$E_{flame} = \eta F_{fuel} \Delta H_{comb} \tag{8}$$

where η considers the combined effects of incomplete conversion during the reaction and energy lost due to the outflow of the combustion mixture and through the reactor walls to the environment, and is considered to be $\eta = 0.64$. Equation 8 assumes that the flow rate of fuel is proportional to the energy the flame produces (i.e., increasing or decreasing the flow rate does not lead to increased or decreased efficiency). The value of the heat of combustion ΔH_{comb} was estimated using heats of formation data Elliott et al. (2012) and Hess's Law to be approximately -58 kJ/mol. In this calculation, it was assumed that combustion occurs for CH_4, CO, and H_2, and that there is excess oxygen to react. In addition, the effects of pressure were neglected, and temperature was considered to have a negligible effect on the heat of combustion.

Since the primary heat transfer method within the combustion chamber is radiation, conduction and convection can be neglected Lao et al. (2016). For radiative heat transfer, the fraction of the energy that is transferred from the source to target can be estimated using the surface area of a sphere extending out around the source. For the SMR simulation, it was assumed that the entire tube is at a constant distance L from the burner. The value of 0.7 m was selected for L based on an examination of the geometry used to simulate a full reforming furnace in Tran et al. (2017a). In addition, it is assumed that the energy is spread out over a half-sphere extending from the reactor wall, as the wall prevents transfer to the opposite half-sphere. The surface area of this half-sphere can be represented as $\frac{1}{2}4\pi L^2$. The tube target is assumed to be in a direct line-of-sight of the burner with an incident area of $2rh$, where $r = 0.073$ m is the tube outer radius and $h = 1$ m is the height of the simulated tube segment. The influence of the angle of the absorbing surface is neglected. This means that the energy that reaches the tube E_{tube} can be represented in the following way:

$$E_{tube} = E_{flame} \frac{2rh}{\frac{1}{2}4\pi L^2} \tag{9}$$

It is assumed that the absorbance of the tube surface is large (near 1) as any reflected heat is subsequently absorbed by nearby tubes, and energy reflected from nearby tubes is absorbed by the considered tube. In addition, it is assumed that there are evenly spaced burners around the pipe each emitting an energy of E_{flame} so that, at any vertical position on the pipe, the energy received by the pipe is constant around the entire circumference. At the same time, it is assumed that, at any given point on the surface of the tube, only one burner is contributing heat.

Next, we assume that the system is in a pseudo steady-state, even during transient operation. Then, based on a balance of energy about the pipe surface, it is assumed that the amount of energy absorbed due to radiation must equal the amount of energy conducted through the pipe wall. Fourier's law is used describe conduction through the pipe wall:

$$E_{tube} = -kA\frac{\overline{T}_{outer} - \overline{T}_{inner}}{\delta_t} \tag{10}$$

where $\overline{T}_{inner}$ and $\overline{T}_{outer}$ are the average temperatures along the inner and outer surfaces of the tube, respectively, $\delta_t = 0.010$ m is the thickness of the tube wall, k is the thermal conductivity of the wall, and A is the area of heat conduction in the wall (assuming $A = 2rh$ so the area of heat radiation and conduction are equal). A value of $k = 29.40$ W/m-k was selected Steel Founders' Society of America (2004), which is identical to the value used in the Fluent simulation.

Five steady-state simulations of the SMR tube were completed using different values of T_{wall}^{max}, and values of $\overline{T}_{inner}$ and $\overline{T}_{outer}$ were determined from these simulations. Plots of T_{wall}^{max} versus $\overline{T}_{inner}$ and $\overline{T}_{outer}$ were then created to find the following linear relations:

$$T_{wall}^{max} = \overline{T}_{outer} + 123.08 \tag{11}$$

$$T_{wall}^{max} = 1.3195\ \overline{T}_{inner} - 127.96 \tag{12}$$

Finally, equations 8, 9, 10, 11, and 12 can be combined to give a relation between F_{fuel} and T_{wall}^{max}:

$$T_{wall}^{max} = \frac{-\eta\delta_t\Delta H_{comb}}{0.4843\pi L^2 k}F_{fuel} + 908.8077 \tag{13}$$

2.5.4. Controller Design

The simplified ARX models were applied in an IPOPT code to simulate the SMR process in four different configurations. In the first configuration, the MPC was designed to adjust T_{wall}^{max} with

the following objective function and constraint:

$$\min_{T_{wall}^{max}(k);k=1,2,\ldots,N} \sum_{i=1}^{N} -x_{H2}(k+i-1) \quad s.t.\ 987K \leq T_{wall}^{max} \leq 1200\ K \tag{14}$$

where N is the MPC prediction horizon (selected to contain 60 sampling periods for all four MPC configurations) and x_{H2} is the outlet hydrogen mole fraction for a 1 m tube. The process was initialized from a steady-state simulated with $T_{wall}^{max} = 1100$ K. At these conditions, the outlet hydrogen mole fraction is 0.427 and the maximum equivalent stress is estimated to be 5.619 $\times 10^9$ Pa. The different time steps for the stress and hydrogen mole faction ARX models need to be reconciled; therefore, it was necessary to apply the stress model 50 times per time step of the hydrogen model. This is necessary because the stress model was developed using data containing time steps of 0.01 seconds and the hydrogen mole fraction model used time steps of 0.5 seconds. The result of this simulation is shown in Figure 20. Since the objective function (in equation 14) seeks to maximize the outlet hydrogen mole fraction, the MPC drives the temperature of the reforming tube wall to the maximum upper bound (where T_{wall}^{max} is 1200 K). This results in a new steady-state with an increased maximum equivalent stress.

The second configuration adds a constraint on the maximum value of the equivalent (von Mises) stress σ_{VM}:

$$\min_{T_{wall}^{max}(k);k=1,2,\ldots,N} \sum_{i=1}^{N} -x_{H2}(k+i-1) \quad s.t.\ 987K \leq T_{wall}^{max} \leq 1200\ K \quad \sigma_{VM} \leq 6 \times 10^9\ Pa \tag{15}$$

The results of this simulation are shown in Figure 21. Similar to the first configuration, the system is driven to a new steady-state. This time, however, the equivalent stress is maintained below the value specified in the constraints as the controller selects a lower value of T_{wall}^{max}.

The third configuration applies the material constraint from equations 6, 7, and 13:

$$\begin{aligned}
&\min_{T_{wall}^{max}(k);k=1,2,\ldots,N} \sum_{i=1}^{N} -x_{H2}(k+i-1) \\
&s.t.\ 987K \leq T_{wall}^{max} \leq 1200\ K \\
MF_{fuel,ave} - &\sum_{j=k}^{min(k+N,M-1)} F_{fuel}(\tau_j) - \sum_{i=0}^{k-1} F_{fuel}^{*}(\tau_j) \\
&\leq max(M-N-k,0)F_{fuel,max} \\
MF_{fuel,ave} - &\sum_{j=k}^{min(k+N,M-1)} F_{fuel}(\tau_j) - \sum_{i=0}^{k-1} F_{fuel}^{*}(\tau_j) \\
&\geq max(M-N-k,0)F_{fuel,min} \\
T_{wall}^{max} &= \frac{-\eta\delta_t\Delta H_{comb}}{0.4843\pi L^2 k}F_{fuel} + 908.8077
\end{aligned} \tag{16}$$

The results of this simulation are shown in Figure 22. It is shown that the controller no longer drives the system to a steady-state. Instead, the controller optimizes the outlet hydrogen mole fraction by first, at the beginning of each operating period, driving the value of T_{wall}^{max} to the upper bound of 1200 K. Then nearing the end of each operating period, the controller selects lower values to ultimately achieve the desired average fuel consumption of $F_{fuel,ave} = 30$ mol/s.

The fourth configuration applies both the maximum stress upper bound constraint and the material constraint:

$$\begin{aligned}
&\min_{T_{wall}^{max}(k);k=1,2,\ldots,N} \sum_{i=1}^{N} -x_{H2}(k+i-1) \\
&s.t.\ 987K \leq T_{wall}^{max} \leq 1200\ K \\
&\sigma_{VM} \leq 6\times 10^9\ Pa \\
MF_{fuel,ave} - &\sum_{j=k}^{min(k+N,M-1)} F_{fuel}(\tau_j) - \sum_{i=0}^{k-1} F_{fuel}^{*}(\tau_j) \\
&\leq max(M-N-k,0)F_{fuel,max} \\
MF_{fuel,ave} - &\sum_{j=k}^{min(k+N,M-1)} F_{fuel}(\tau_j) - \sum_{i=0}^{k-1} F_{fuel}^{*}(\tau_j) \\
&\geq max(M-N-k,0)F_{fuel,min} \\
T_{wall}^{max} &= \frac{-\eta\delta_t\Delta H_{comb}}{0.4843\pi L^2 k}F_{fuel} + 908.8077
\end{aligned} \tag{17}$$

The results of this simulation are shown in Figure 23 and are similar to the previous case, where

the hydrogen mole fraction will decrease near the end of each operating period. The difference is the maximum stress will be at most 6×10^9 Pa.

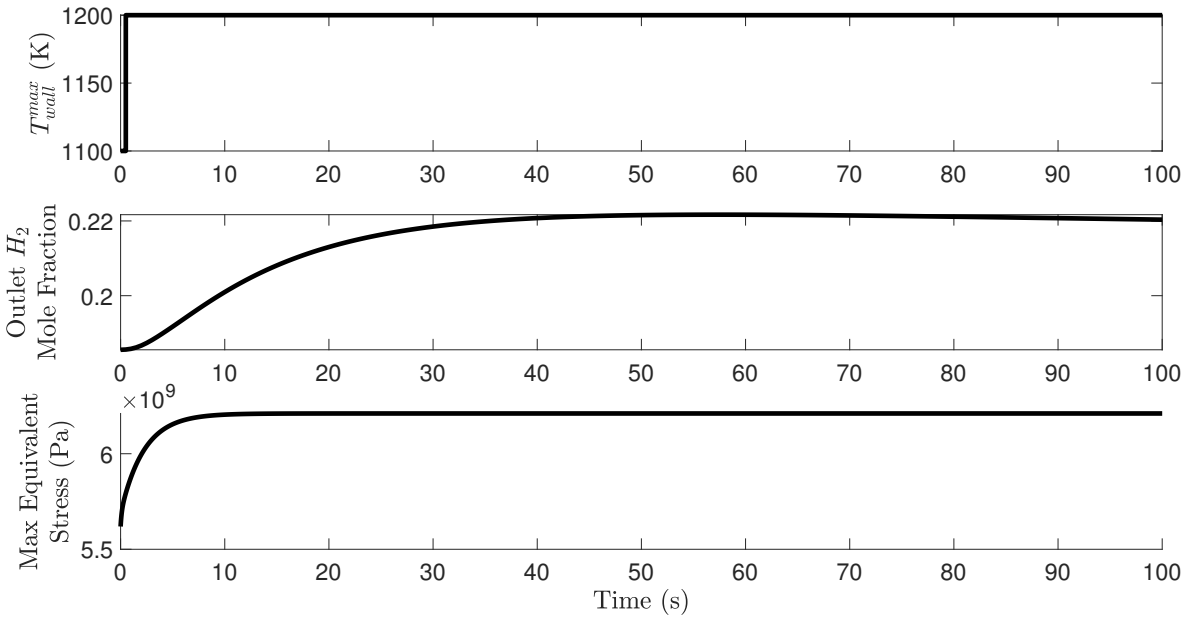

Figure 20: Results of IPOPT code for MPC with a constraint that bounds T_{wall}^{max}.

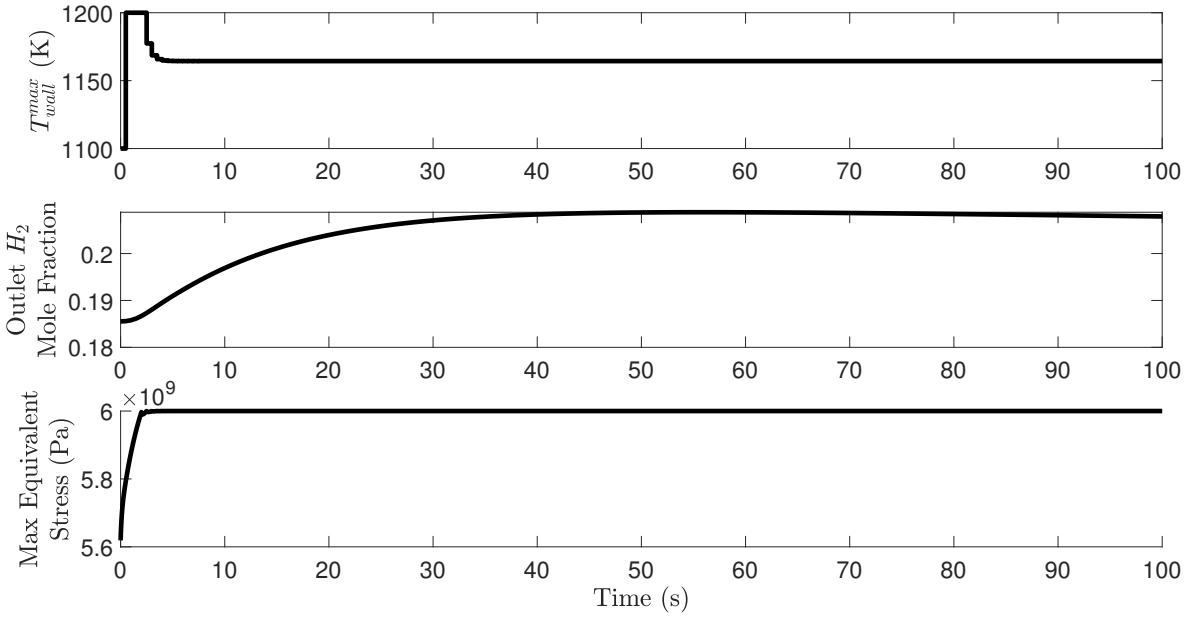

Figure 21: Results of IPOPT code for MPC with constraints on T_{wall}^{max} and the maximum equivalent (von Mises) stress.

There is potential for fluid and solid mechanics simulations to act as a test bed to offer the abil-

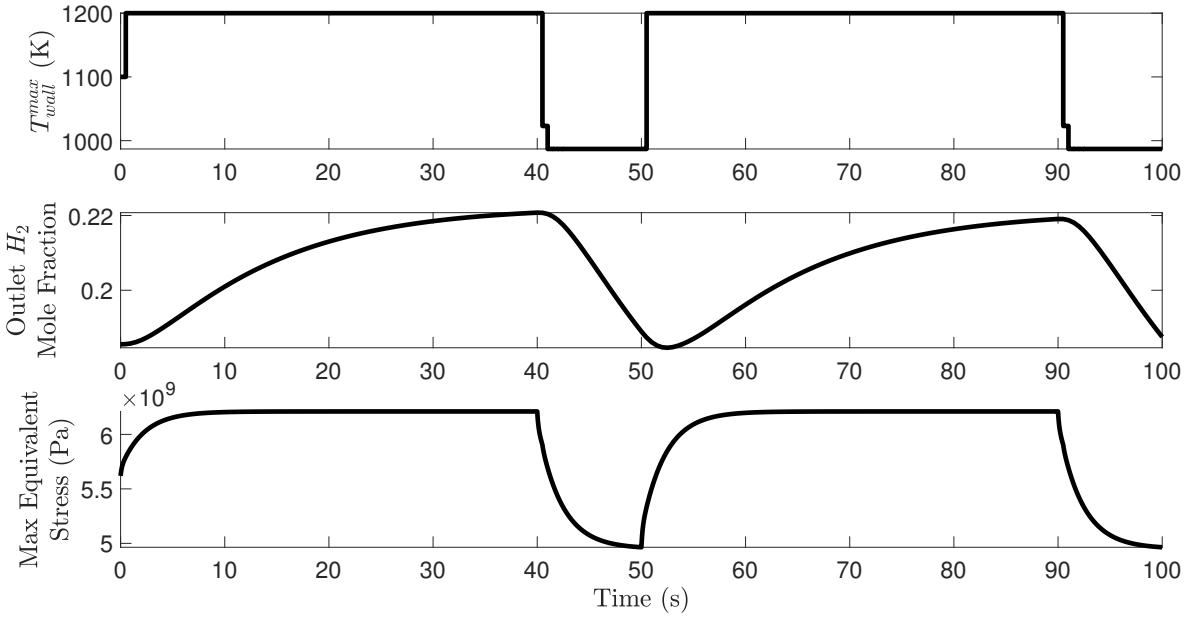

Figure 22: Results of IPOPT code for MPC with a constraint that bounds T_{wall}^{max} and a material constraint that ensures the average fuel consumption remains constant.

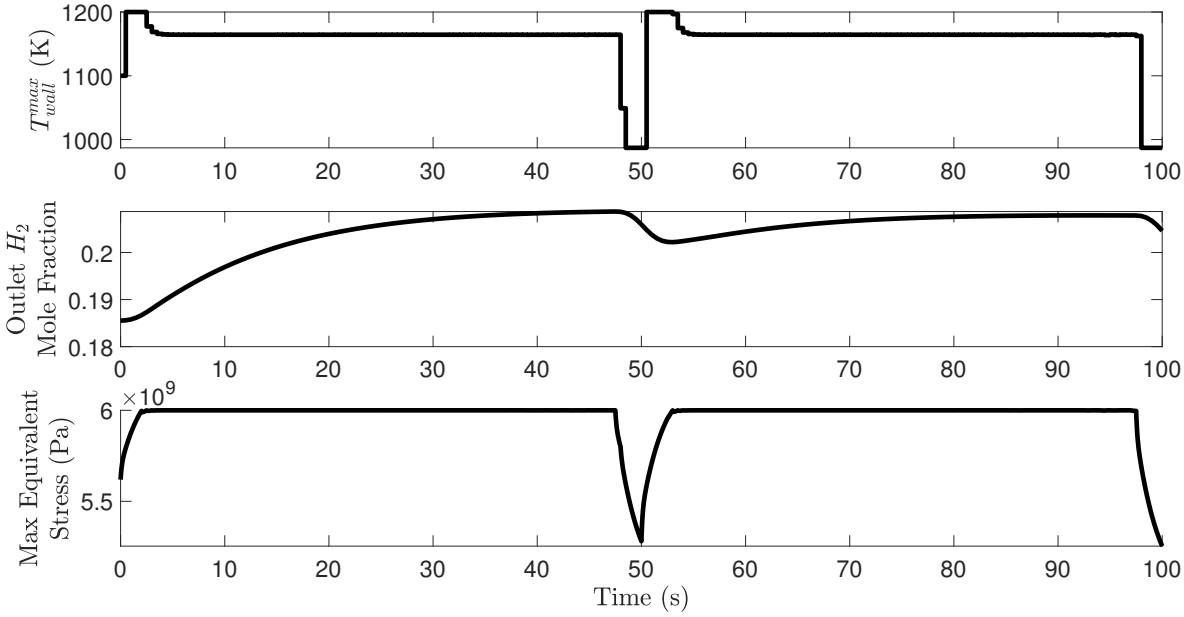

Figure 23: Results of IPOPT code for MPC with a constraint that bounds T_{wall}^{max}, a constraint limiting the maximum equivalent (von Mises) stress, and a material constraint that ensures the average fuel consumption remains constant.

ity to gain a deeper understanding of how cyberattacks can affect a process and a control system. Through applying test attacks through simulation, one can probe for weaknesses in process equipment and control systems. In addition, such simulations could be simplified using reduced-order

models and still yield important information about the process under control from an equipment perspective. Though the case studies presented are simplified, they suggest that this methodology could be helpful in the process systems engineering and control community in cases where more complex equipment is present and the impacts of the control actions on the equipment is unclear, or where it is desired to use this type of methodology as part of a safety study.

Remark 3. *In the MPC simulations, the data-driven models are assumed to fully represent the plant (i.e., plant/model mismatch and sensor noise are not considered). If an MPC strategy based on a reduced-order model was implemented at a real plant, however (or even potentially on the CFD/FEA system), plant/model mismatch would be expected. However, if the plant/model mismatch is sufficiently small, MPC would still be expected to produce reasonably accurate state predictions for maximizing the objective function and seeking to meet constraints, but hard constraints may become infeasible due to the mismatch so that slack variables or a soft constraint may be needed.*

3. Control-Theoretic Safety: Meeting Theoretical Requirements

The discussion above focused on dynamic operation for safety when equipment is considered. This section considers dynamic operation for safety when theory is considered. In our prior work (e.g., Rangan et al. (2021); Oyama and Durand (2020a)) we have developed control-theoretic guarantees for safety (at least for some time period) after a cyberattack on a specific control design known as Lyapunov-based economic model predictive control (LEMPC) Heidarinejad et al. (2012). However, the control-theoretic guarantees rely on many parameters which are not necessarily simple to obtain for a system. For the purpose of evaluating cyberattack detection policies integrated with control, it is desirable to develop strategies for providing confidence that the parameters and functions used in a simulation study related to such a topic meet the required theoretical properties (i.e., do not have vulnerabilities), or that at least they meet the theoretical requirements for many conditions that might occur in the simulation (i.e., there is a rationale for using them in seeking to understand properties of strategies for detecting cyberattacks in a simulation). Currently, an appropriate strategy for achieving this has not been developed.

In Oyama et al. (2022), we provided an initial study for evaluating whether the parameters of an

LEMPC that meet the theory that guarantees safety might be obtained. We did this in the context of the baseline LEMPC design (not cyberattack-resilient) from Heidarinejad et al. (2012) as a first step toward moving toward obtaining parameters for a form integrated with cyberattack detection. This prior study was limited in that it looked at only a single Lyapunov-based control design, focusing on obtaining the parameters through worst-case analyses and a guess-and-check policy for selecting functions of the control design. Despite these limitations, it indicated that for the selected control law and other functions, LEMPC may be difficult to implement practically (e.g., it may require a sampling period Δ on the order of 10^{-10} h or less for the example considered in Oyama et al. (2022)). However, it remains unclear from these initial studies how to systematically locate the parameters and functions required for meeting all of the theoretical requirements of an LEMPC, and it remains unclear whether there would exist other combinations of functions and parameters that might do better than what was previously reported (in the sense that it might enable a more realistic sampling period to be used). For example, it is reasonable to ask whether the "guess-and-check" policy for selecting functions to be used in finding the parameters of the control law that meet the theory is the best that can be done, or if there is an alternative computational way to "find" such functions. This section seeks first to further analyze the benefits and limitations of a "guess-and-check" policy and subsequently to propose and evaluate an alternative optimization-based concept for searching for appropriate parameters and functions for the LEMPC. Though the focus is on LEMPC without the additional complications of extending the analysis to consider cases involving cyberattacks, we view this analysis as a first step toward identifying a route for simulating versions of LEMPC that have been designed in tandem with cyberattack detection policies.

This section begins with a description of the theory of LEMPC, which sets the stage for a motivating example that demonstrates that despite the ability to perform analyses of approximate best-case values of Δ for a variety of Lyapunov functions and Lyapunov-based controllers with an approach following that in Oyama et al. (2022), guessing and checking functions for an LEMPC can leave it unclear whether there exist any combinations of functions and parameters that can outperform those located through a guess. This leads to the analysis in the subsequent section of the potential of setting up an optimization problem to "find" parameters and functions meeting

the stability theory requirements while seeking to maximize the sampling period length. How to formulate a version of such an optimization problem is not obvious, as there are many considerations that must be taken into account, including how to deal with computation time, how to add constraints to the optimization problem that prevent undesirable behavior of the unknown functions and parameters, and how to evaluate solutions to the complex problem (particularly if they may not be global minima due to the use of a local nonlinear optimizer and a coarse state and input space discretization used in the optimization problem). We discuss concepts for formulating such an optimization problem, and present results and discussion to evaluate their performance and compare the optimization-based approach with the "guess-and-check" approach.

3.1. Meeting Control-Theoretic Safety Requirements: Preliminaries

3.1.1. Notation

The vector Euclidean norm is represented by $|\cdot|$. A function is of class $\mathcal{K}$ if it is a strictly increasing function $\alpha : [0, a) \to [0, \infty)$ with $\alpha(0) = 0$. The transpose of a vector x is denoted by x^T. The notation " / " signifies set subtraction $x \in A/B := \{x \in R^n : x \in A, x \notin B\}$). A level set of a positive definite function V is represented by $\Omega_\rho := \{x \in R^n : V(x) \leq \rho\}$. We define a sampling time as $t_k := k\Delta$, $k = 0, 1, \ldots$, where Δ is a sampling period.

3.1.2. Class of Systems

This work considers nonlinear systems of the form:

$$\dot{x}(t) = f(x(t), u(t), w(t)) \tag{18}$$

where the state, input, and disturbance vectors are denoted by $x \in X \subset R^n$, $u \in U \subset R^m$ ($u = [u_1, \ldots, u_m]^T$), and $w \in W \subset R^z$, respectively, where $W := \{w \in R^z \ : \ |w| \leq \theta, \ \theta > 0\}$. When $w \equiv 0$, Eq. 18 is referred to as the nominal system. f is considered to be a locally Lipschitz function of its arguments with $f(0, 0, 0) = 0$.

In this work, we consider the nominal system ($w \equiv 0$) which is stabilizable through the application of an asymptotically stabilizing feedback control law $h(x)$, a sufficiently smooth Lyapunov function $V(x)$, and class $\mathcal{K}$ functions $\alpha_i(\cdot), i = 1, 2, 3, 4$, where, $\forall x \in D \subset \mathbb{R}^n$ (D is an open

neighborhood of the origin):

$$\alpha_1(|x|) \leq V(x) \leq \alpha_2(|x|) \tag{19a}$$

$$\frac{\partial V(x)}{\partial x} f(x, h(x), 0) \leq -\alpha_3(|x|) \tag{19b}$$

$$\left| \frac{\partial V(x)}{\partial x} \right| \leq \alpha_4(|x|) \tag{19c}$$

$$h(x) \in U \tag{19d}$$

$\Omega_\rho \subset D$ is defined as the stability region of the nominal closed-loop system under the Lyapunov-based controller $h(x)$ and is chosen so that $x \in X, \forall x \in \Omega_\rho$.

Because V is a sufficiently smooth function and f is locally Lipschitz, we can say the following $\forall x_1, x_2 \in \Omega_\rho, u, u_1, u_2 \in U$, and $w \in W$:

$$|f(x_1, u_1, w) - f(x_2, u_2, 0)| \leq L_x|x_1 - x_2| + L_u|u_1 - u_2| + L_w|w| \tag{20a}$$

$$\left| \frac{\partial V(x_1)}{\partial x} f(x_1, u_1, w) - \frac{\partial V(x_2)}{\partial x} f(x_2, u_2, 0) \right| \leq L_x^{'}|x_1 - x_2| + L_u^{'}|u_1 - u_2| + L_w^{'}|w| \tag{20b}$$

$$|f(x, u, w)| \leq M \tag{21}$$

where $L_x, L_x^{'}, L_u, L_u^{'}, L_w, L_w^{'}$, and M are positive constants.

3.1.3. Lyapunov-based Economic Model Predictive Control (LEMPC)

This work considers a control law known as LEMPC Heidarinejad et al. (2012) defined by:

$$\min_{u(t) \in S(\Delta)} \quad \int_{t_k}^{t_{k+N}} [L_e(\tilde{x}(\tau), u(\tau))] d\tau \tag{22a}$$

$$\text{s.t.} \quad \dot{\tilde{x}} = f(\tilde{x}(t), u(t), 0) \tag{22b}$$

$$\tilde{x}(t_k) = x(t_k) \tag{22c}$$

$$\tilde{x}(t) \in X, \, \forall \, t \in [t_k, t_{k+N}) \tag{22d}$$

$$u(t) \in U, \; \forall \, t \in [t_k, t_{k+N}) \tag{22e}$$

$$V(\tilde{x}(t)) \leq \rho_e, \;\; \forall \, t \in [t_k, t_{k+N}), \quad \text{if} \;\; x(t_k) \;\in\; \Omega_{\rho_e} \tag{22f}$$

$$\frac{\partial V(x(t_k))}{\partial x} f(x(t_k), u(t_k), 0) \;\leq \frac{\partial V(x(t_k))}{\partial x} \, f(x(t_k), h(x(t_k)), 0)$$
$$\text{if} \;\; x(t_k) \notin \Omega_{\rho_e} \tag{22g}$$

where $L_e(\cdot,\cdot)$ is the LEMPC stage cost (Eq. 22a), $u \in S(\Delta)$ signifies that u is a piecewise-constant input trajectory with period Δ, and the prediction horizon is denoted by N. Eqs. 22d and 22e represent state and input constraints, respectively, whereas Eqs. 22f-22g are Lyapunov-based stability constraints.

3.1.4. Closed-Loop Stability Under LEMPC

The theoretical conditions required for LEMPC to guarantee safety from Heidarinejad et al. (2012) are noted in Theorem 1 below, which utilizes notation presented in the two following propositions.

Proposition 1. *Mhaskar et al. (2012); Heidarinejad et al. (2012) Consider the following two systems:*

$$\dot{x}_a = f(x_a(t), u(t), w(t)) \tag{23a}$$

$$\dot{x}_b = f(x_b(t), u(t), 0) \tag{23b}$$

with initial states of $x_a(t_0) \in \Omega_\rho$ and $x_b(t_0) \in \Omega_\rho$ ($x_a(t_0) = x_b(t_0)$). There exists a class $\mathcal{K}$ function $f_W(\cdot)$ that satisfies the following equations $\forall\ x_a, x_b \in \Omega_\rho$ and $\forall\ w \in W$:

$$|x_a(t) - x_b(t)| \leq f_W(t - t_0) \tag{24a}$$

$$\text{where } f_W(\tau) := \frac{L_w \theta}{L_x}(e^{L_x \tau} - 1) \tag{24b}$$

Proposition 2. *Mhaskar et al. (2012); Heidarinejad et al. (2012) For the Lyapunov function $V(\cdot)$ of the nominal system in equation Eq. 18, we can find a function $f_V(\cdot)$ which satisfies:*

$$V(x) \leq V(\hat{x}) + f_V(|x - \hat{x}|) \tag{25a}$$

$$\text{where } f_V(s) := \alpha_4(\alpha_1^{-1}(\rho))s + M_v s^2 \tag{25b}$$

$\forall\ x, \hat{x} \in \Omega_\rho$, where M_v is a positive constant.

Theorem 1. *Heidarinejad et al. (2012) Consider the system of Eq. 18 in closed-loop under the LEMPC design of Eq. 22 based on a controller $h(x)$ that satisfies the conditions of Eq. 19. Let $\epsilon_w > 0$, $\Delta > 0$, and $\rho > \rho_e > \rho_{\min} > \rho_s > 0$ satisfy:*

$$\rho_e \leq \rho - f_V(f_W(\Delta)) \tag{26}$$

and

$$-\alpha_3(\alpha_2^{-1}(\rho_s)) + L_x' M\Delta + L_w'\theta \leq -\epsilon_w/\Delta \tag{27}$$

If $x(t_0) \in \Omega_\rho$ *and* $N \geq 1$ *where*

$$\rho_{\min} = \max\{V(x(t)) : \ t \in [t_k, t_{k+1}),\ V(x(t_k)) \leq \rho_s,\ u \in U,\ w \in W\} \tag{28}$$

then the state $x(t)$ *of the closed-loop system is always bounded in* Ω_ρ *and is ultimately bounded in* $\Omega_{\rho_{\min}}$.

In the following section, we probe a process example to showcase challenges with obtaining the parameters and functions in the theory above.

Remark 4. *The control theory discussed above is for a case that considers bounded plant/model mismatch, but no measurement noise. However, extensions can be made to also include measurement noise (for example, the work on cyberattack detection for a process under LEMPC in Oyama and Durand (2020a) considers measurement noise). No measurement noise will be considered in this work.*

3.2. Motivation for Searching for Parameters and Functions of LEMPC Through Optimization

In this section, we discuss an example that motivates our subsequent investigation of an optimization-based procedure for attempting to obtain parameters for an LEMPC satisfying the conditions of Propositions 1-2 and Theorem 1 for a CSTR, as a step moving toward systematically obtaining such parameters for process systems motivated by safety considerations.

A non-isothermal, well-mixed continuous stirred-tank reactor (CSTR) is considered in this simulation, which has an inlet and outlet stream and is equipped with a jacket to add or remove heat. An irreversible, exothermic, second-order reaction of $A \rightarrow B$ occurs in the reactor. Reactant A is fed to the reactor at a volumetric flow rate of $F = 5.0\ m^3/h$ with a temperature of $T_0 = 300\ K$ in an inert solvent with concentration C_{A0}. The reactor holds a liquid volume of $V_t = 1.0\ m^3$, which is assumed constant, and the jacket provides/removes heat at a rate of Q. The liquid has a density of $\rho_L = 1000\ kg/m^3$ and a heat capacity of $C_p = 0.231\ kJ/kg\ K$, which are assumed to be constant.

The dynamic model of the CSTR is represented using the following equations developed from mass and energy balances:

$$\frac{dC_A}{dt} = \frac{F}{V_t}(C_{A0} - C_A) - k_0 e^{-E/RT} C_A^2 \tag{29a}$$

$$\frac{dT}{dt} = \frac{F}{V_t}(T_0 - T) - \frac{\Delta H k_0}{\rho_L C_p} e^{-E/RT} C_A^2 + \frac{Q}{\rho_L C_p V_t} \tag{29b}$$

where reactor temperature and concentration of A are represented using T and C_A, respectively. Values of $k_0 = 8.46 \times 10^6\ m^3/h\ kmol$, $E = 5.0 \times 10^4\ kJ/kmol$, and $\Delta H = -1.15 \times 10^4\ kJ/kmol$ are used for the pre-exponential factor, activation energy, and the enthalpy of the reaction, respectively. The parameters are summarized in Table 4.

Table 4: Parameters for the CSTR model.

Parameter	**Value**	**Unit**
V_t	1	m^3
T_0	300	K
C_p	0.231	kJ/kg·K
k_0	8.46×10^6	m^3/h·kmol
F	5	m^3/h
ρ_L	1000	kg/m^3
E	5×10^4	kJ/kmol
R	8.314	kJ/kmol·K
ΔH	-1.15×10^4	kJ/kmol

For the simulation of the CSTR, C_{A0} and Q are treated as manipulated inputs to the process, with bounds of $0.5 \leq C_{A0} \leq 7.5\ kmol/m^3$ and $-5.0 \times 10^5 \leq Q \leq 5.0 \times 10^5\ kJ/hr$, and T and C_A are the process states. An open-loop asymptotically stable steady-state occurs at $C_{As} = 1.2\ kmol/m^3$ and $T_s = 438.2\ K$, where the subscript s indicates the steady-state values. In the control formulation, the state and input vectors are represented using deviation variables as $x^T = [C_A - C_{As} \quad T - T_s]$ and $u^T = [C_{A0} - C_{A0s} \quad Q - Q_s]$, respectively.

In our prior work Oyama et al. (2022), we provided an initial attempt at locating parameters of an LEMPC for this process that might meet the conditions required for the theoretical guarantees. This initial approach involved selecting a Lyapunov function, Lyapunov-based controller, and specific forms of α_1, α_2, α_3, and α_4, and then obtaining approximations of parameters in Propositions 1-2

and Theorem 1 using a brute force method in which the state-space was discretized and values of the parameters consistent with the points tested in state-space were obtained. This does not guarantee that values of the parameters that meet all of the theoretical requirements (including at points outside of the discretization) were selected, but it does provide a maximum potential order of magnitude of Δ that meets Eq. 27 if there are no disturbances for a given set of functions V, h, and α_j, $j = 1, 2, 3, 4$. The benefit of this is that if this approximate "best-case" value of Δ is already too small to be reasonable for a given application, then this provides an indication that the selected V, h, and α_j, $j = 1, 2, 3, 4$ may not be selected if it is desired for the LEMPC to have its theoretical guarantees (and there is no guarantee that there is any LEMPC design that would satisfy a certain requirement on Δ). However, there is still some approximation in this method if parameters are rounded up or down once found, so that the "best-case" approximation depends on this degree of rounding.

For several values of ρ tested in Oyama et al. (2022), the order of magnitude of Δ would have been 10^{-10} h or less. This could pose challenges for practical implementation of LEMPC (i.e., finding sensors with such a small sampling period may be challenging, and this represents only a "best case" value of Δ so that it is possible that a smaller value might be required). The work in Oyama et al. (2022) was limited to a case study with only a few permutations of the large set of possible functions and parameters available in seeking to design an LEMPC; therefore, it is not clear if there may be a way to adjust other aspects of an LEMPC besides those performed in Oyama et al. (2022) to provide a more attractive upper bound on Δ (for example, V or h could be changed compared to what was tested in Oyama et al. (2022)). In this section, we seek to investigate how changes to various aspects of an LEMPC might be made in seeking to (loosely) "optimize" the value of Δ, and discuss benefits and challenges of this method to motivate the investigation of a more formal optimization-based approach in the subsequent section.

We first want to investigate the role of the choice of $V(x)$ in the size of the parameters of the LEMPC, and whether different choices of $V(x)$ have an impact on the apparent maximum value of Δ. Therefore, whereas in Oyama et al. (2022), we used $V(x) = x^T P x$ where $P = [2000\ -10;\ -10\ 3]$, in this section, we will first try $P = [20\ -10;\ -10\ 50]$. The shape of this new stability region in

state-space in this case is shown in Fig. 24. This figure also reflects whether $\dot{V}$ is negative at the points tested in state-space in the plot ($h(x)$ was designed such that the component corresponding to u_1 is set to 0 kmol/m^3 and the component corresponding to u_2 is set via Sontag's control law Lin and Sontag (1991)). The points tested are those in a discretized state-space where C_A varies in increments of 0.1 kmol/m^3 between 0 and 4 kmol/m^3, while T varies in increments of 0.1 K between 435 and 441 K. The ellipse corresponds to $\rho = 20$. It is contained within the gray region, which is where $\dot{V}$ is negative. The white region is a region where $\dot{V}$ is not negative. The impact of this choice of V on the parameters of an LEMPC, compared to what was obtained in Oyama et al. (2022) with a different V, will now be investigated.

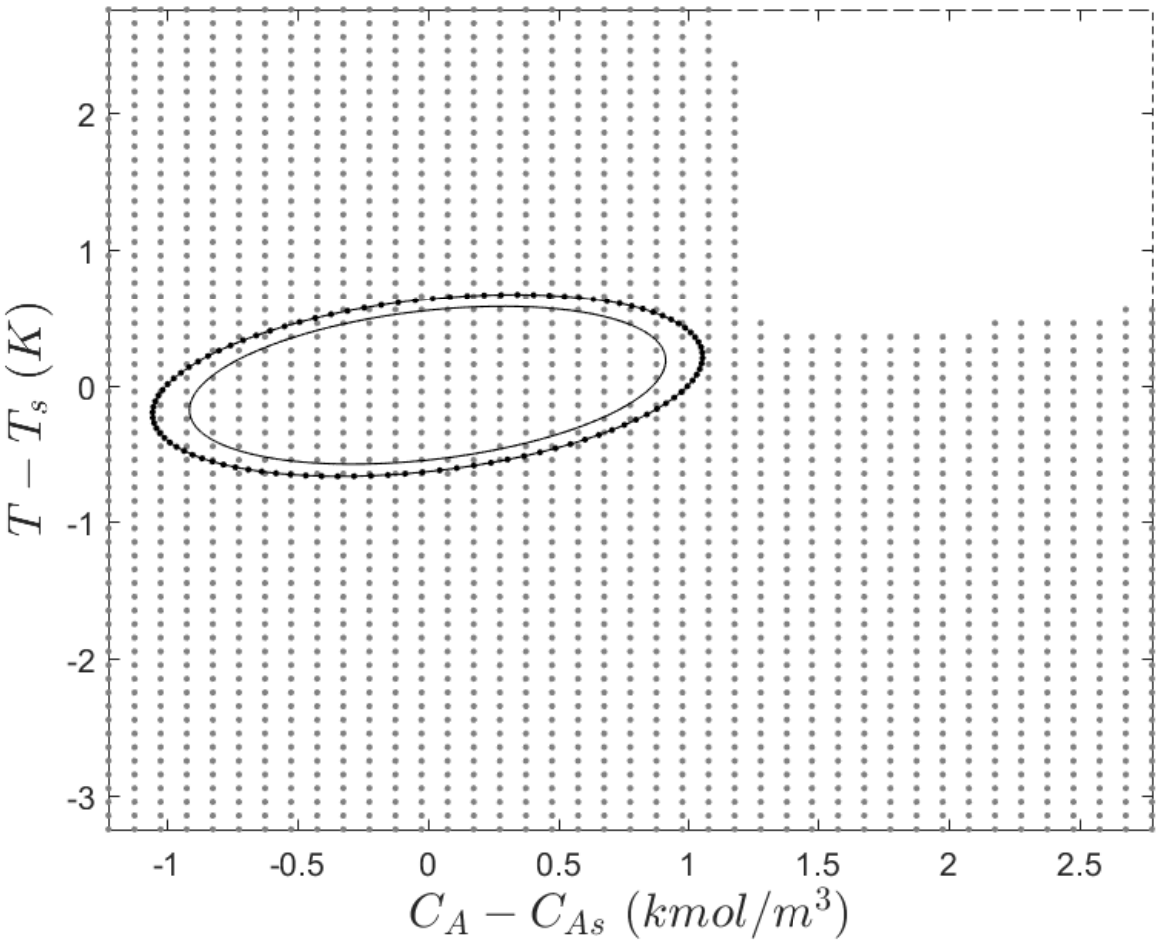

Figure 24: Stability region shape for $V(x) = x^T P x$ with $P = [20\ \ -10;\ \ -10\ 50]$.

We utilize the same procedure as in Oyama et al. (2022) to obtain the parameters for the

LEMPC in Table 5. Specifically, we set $\alpha_1(|x|) = a_1|x|^2$ and $\alpha_2(|x|) = a_2|x|^2$, where $a_1 < \lambda_{\min}(P)$ and $a_2 > \lambda_{\max}(P)$, with $\lambda_{\min}(P)$ and $\lambda_{\max}(P)$ as the maximum and minimum eigenvalues of P, which for this case are 16.9722 and 53.0278, respectively. Then, for points in the same discretization as shown in Fig. 24, the value of a_3 was found by setting it to be less than the value of a_3 obtained when $\alpha_3(|x|) = a_3|x|^2$ and a_3 was decreased from 100 to be set equal to $-\dot{V}/|x|^2$ at any point in the discretization where $\dot{V}$ was greater than $-\alpha_3(|x|)$. This reduced a_3 to 80.0529, so that the value of a_3 to be used according to Table 5 was selected to be 80.

Table 5: First set of parameters for CSTR model.

Parameter	**Value**
ρ	20
a_1	16.5
a_2	53.5
a_3	80
a_4	1810
M	3735
L_x	2010
L_w	0
L'_x	374710
L'_w	0
M_v	10^{-5}
θ	0

Next, α_4 was selected to take the form $a_4|x|^2$. With the same state-space discretization as in Fig. 24, a_4 was initially set to -100 and then changed to $\left|\frac{\partial V}{\partial x}\right| /|x|^2$ whenever $\left|\frac{\partial V}{\partial x}\right| > \alpha_4(|x|)$. This gave a value of a_4 of 1808.125 among the points tested, so a value of 1810 was selected in Table 5. Next, M was determined using the discretization in Fig. 24 for the states, units of 0.5 kmol/m^3 for the range of C_{A0} and units of 10^5 kJ/h for the range of Q. This gave a value of M of 3733.33, so that a value of 3735 was selected in Table 5. Then, L_x and L_w were determined individually by changing only the state in Eq. 20a (for L_x) and then checking that Eq. 20a holds, and setting L_w to 0 since no disturbances are considered. L'_x and L'_w were determined in a similar fashion, but to satisfy Eq. 20b. Finally, M_v was determined to satisfy Eq. 25b.

In Oyama et al. (2022), Eq. 22g was implemented as $-a_3\frac{\rho_s}{a_2}+L'_xM\Delta+L'_w\theta+\bar{\epsilon}_w \leq 0$, in accordance

with Eqs. 24b, 25b, 26, and 27, for determining a best-case order of magnitude of Δ. A best-case here would give that Δ can be no larger than about 2.14×10^{-8} h in this case (if $\rho_s = \rho$ and $\bar{\epsilon}_w$ is small (10^{-5})). At first this seems to be an improvement compared to Oyama et al. (2022) by about two orders of magnitude, but it is difficult to tell as this result is dependent on the (incomplete) discretization and any approximation in parameters in Table 5 or Oyama et al. (2022) and therefore is only an approximate best case (e.g., it is possible that in one or both cases, Δ may need to be smaller, so that which is "better" cannot be seen from this analysis).

Here again we see that L'_x and M are large, which causes the term $\frac{-a_3\rho_s}{a_2}$ to be required to be very large in order to overcome those terms. While this term depends on V and h, as does L'_x, the terms also depend on the input bounds (including M, which can be made arbitrarily small by requiring that the system operate almost exactly at the steady-state). We could therefore consider the impact of changing the input bounds on this problem.

The analysis above shows the impacts of different design decisions on the best-case sampling period of an LEMPC, where even the best-case values are not guaranteed to be reflective of the true bound on Δ if the discretizations used in computing the values of the parameters in Table 5 were modified. One could argue that perhaps global optimization might aid in finding these parameters in an improved fashion (e.g., finding the maximum bound on f when $x \in \Omega_\rho$, $u \in U$, and $w \in W$ for Eq. 21). However, even if more exact values were obtained, this would not solve the issue at hand; specifically, it would not provide clarity on whether a different V, h, or α_j, $j = 1, 2, 3, 4$, could provide a larger value of Δ. If, for example, we had a target magnitude of Δ of approximately 10^{-6} h, this does not aid in identifying whether there exist any functions that can give this (even for the best case); it makes the question one which must be answered by repeated guessing and checking, which is an inefficient approach and may not even turn out to be fruitful as the existence of the function and parameters for hitting the target Δ is not established.

In the discussion above and in Oyama et al. (2022), the same Lyapunov-based controller was used. We now evaluate whether adjusting this controller could have any benefits for adjusting Δ toward a target value. Specifically, we select to use a linear quadratic regulator (LQR) Griffith (2018), where the Lyapunov function V and stabilizing controller $h = -Kx$ are designed around

a linearized process model and controller parameters chosen in a spirit similar to Oyama et al. (2022). The process model used in the LQR is as follows:

$$\dot{x} = Ax + Bu \tag{30}$$

where $A = \frac{\partial f(0,0)}{\partial x}$ and $B = \frac{\partial f(0,0)}{\partial u}$ (i.e., the linearizations of the process model at the origin with respect to the states and inputs). The LQR seeks to minimize a quadratic cost function that is a time integral of $x^T Q x + u^T R u$, where Q and R are weighting matrices used to balance the cost of off-steady state operation and control action, respectively. The weight matrix P for the quadratic Lyapunov function $V = x^T P x$ is found as the solution to the Riccati equation, where $A^T P + PA - PBR^{-1}B^T P + Q = 0$. The LQR controller is formulated as a feedback controller where the gain matrix is computed as $K = R^{-1}B^T P$. In our simulations, $Q = [20\ \ -10;\ \ -10\ 70]$ and $R = [200\ \ -10;\ \ -10\ 60]$, and the lqr function in MATLAB is used.

In finding the best-case value of Δ when the LEMPC uses the LQR, we again neglect disturbances and use a similar procedure to that performed for the other stabilizing control law above. Specifically, class $\mathcal{K}$ functions α are taken to be the product of a coefficient with the squared norm of the states. The coefficients for a_1 and a_2 are taken to be the minimum and maximum eigenvalues of the Lyapunov matrix P, respectively. a_3 is initialized at 10^6 and decreased, following the procedure described above. M is the maximum value of the right-hand side of the nonlinear system within the stability region and under the control actions in the discretization (expanded so that the temperature goes from 430 to 450 K). The Lipschitz constant L'_x is calculated according to the procedure described above. This gives the values in Table 6.

With these new parameters, we again evaluate Δ using the equation $-a_3\frac{\rho_s}{a_2} + L'_x M\Delta + \bar{\epsilon}_w \leq 0$, with $\bar{\epsilon}_w$ considered to be a small number (for a best-case Δ, we will consider it to be 0), and $\rho_s = \rho$ (and disturbances have been neglected). This gives that Δ will be approximately 5.74×10^{-9} h or less. Whether this is an improvement compared to other possibilities is difficult to say as the values of the parameters are obtained using different discretizations in state-space, and this is only an approximate best-case based on the incomplete discretization used and any other approximations or roundings used in obtaining the parameters.

Table 6: Second set of parameters for CSTR model.

Parameter	**Value**
ρ	20
a_1	0.74
a_2	568
a_3	68
M	2464
L'_x	169,264
θ	0

The analysis above indicates that the method for locating a "best-case" Δ that was presented in Oyama et al. (2022) and then summarized and further probed above has benefits and disadvantages. It can serve well as a quick screening method for whether certain functions and the parameters associated with these developed from brute-force checking of functions along an (even potentially coarse) discretization of the state-space would lead to values of Δ that are too small to be used with a sensor that is available for the process. However, they do not make clear how to solve the inverse problem of specifying a sensor's possible sampling rate and then seeking to find the functions with satisfy this requirement. It does not appear intuitive from the analysis above how to modify functions such as V or h to achieve a specific target; the guess-and-check policy used above can be employed, but this is not guaranteed to find solutions. This motivates the investigation in the next section of developing an optimization problem for attempting to locate functions and parameters that can meet the "constraints" of the theory of LEMPC.

Remark 5. *The discussion regarding obtaining Δ indicates that its value is highly impacted by the process dynamics. For example, a process with a larger value of M (i.e., $|f|$ is larger) will require Δ to be smaller for the same magnitude of $L'_x M\Delta$. This indicates that process design can impact the feasibility of obtaining safety guarantees (and control-theoretic guarantees on cyberattack-resilience) using Lyapunov-based economic model predictive control. Furthermore, the sensing devices chosen (which may have certain sampling rates possible) also impact whether the guarantees can be developed for a given design. This indicates the importance of considering safety in a control-theoretic sense at the design stage of a process, complementing the work on computational fluid dynamics and finite*

element analysis that indicated that the impacts of control on equipment could also be an important part of the design protocols for a system at the HAZOP stage.

Remark 6. *It should be noted that even if LEMPC is not able to provide a sufficiently large sampling period for the use of a given sensor, this does not necessarily mean that another control law can. For example, instead of considering only the region of attraction (which we define to be the set of points in state-space from which there exist input trajectories with the inputs in the input bounds which could drive the closed-loop state to the origin under continuous implementation of the controller), one could consider the region of attraction for sample-and-hold controller implementation (i.e., the set of states from which there exist sample-and-hold input trajectories with the inputs in the input bounds which could drive the closed-loop state toward the origin). Depending on the process dynamics and sampling period selected, it is possible that this set is empty or very small, indicating that control objectives could not be achieved with the given process dynamics and desired sampling period, regardless of whether LEMPC was used or not. A test of the conservativeness of LEMPC is to see, for a given controller parameterization, how large the stability region of the LEMPC is compared to the region of attraction for sample-and-hold control law implementation.*

3.3. Searching for Parameters and Functions of LEMPC Through Optimization: Investigation Through a Chemical Process Example

In this section, we utilize the same chemical process example as in the prior section to develop and analyze an optimization-based strategy for obtaining parameters and functions of LEMPC that have a relationship to the theoretical conditions. The discussion above indicates that it can be difficult to find functions/parameters of an LEMPC that provide theoretical guarantees while also enabling reasonable values of Δ to be used. Therefore, we are interested in developing an optimization problem that can maximize the value of Δ that would satisfy the various constraints.

How to develop an optimization problem for seeking to achieve all of the goals of the theory requires consideration. Therefore, we will now describe principles behind its construction to provide insight into tradeoffs and opportunities in creating such a formulation. We would like to find a suitable $V(x)$ and $h(x)$ combination simultaneously by designing an optimization problem according to the constraints of Section 3.1.4. Specifically, we would like to propose potential forms for key

functions in Section 3.1.4 (V, h, and α_j, $j = 1, 2, 3, 4$) and use the optimization problem to find coefficients of the terms in the functional forms that we select that cause the requirements of Section 3.1.4 to be met. However, as discussed above, we would like to meet these requirements without requiring Δ to be too small.

The first step in developing this method is to choose the potential components of the key functions, namely the class $\mathcal{K}$ functions (α_1, α_2, α_3, and α_4) and the functions $V(x)$ and $h(x)$, where the coefficients multiplying the terms in these functions will be decision variables of the problem, with the intent of enabling the optimization problem to locate viable forms of V, and h, or the various α_j (inspired by the procedure for obtaining terms in a data-driven model in Brunton et al. (2016)). Special consideration is made in the selection of the possible forms of the functions to ensure the intended form of each equation is found. For example, the α functions must be designed to be strictly increasing with $\alpha(0) = 0$. Therefore, we consider $\alpha_1(s) = a_1 s + a_2 s^2 + a_3 s^4$, which does not include terms that may not meet the class $\mathcal{K}$ conditions such as $sin(s)$. In addition, $\alpha_2(s) = b_1 s + b_2 s^2 + b_3 s^4$, $\alpha_3(s) = c_1 s + c_2 s^2 + c_3 s^4$, and $\alpha_4(s) = d_1 s + d_2 s^2 + d_3 s^4$, for the same reasons. To ensure that V has a form that could be positive definite, it is guessed to have the form $V(x) = v_1 x_1^2 + v_2 x_2^2 + v_3 x_1^4 + v_4 x_1^2 x_2^2 + v_5 x_2^4$. Finally, $h(x)$ is given two components ($h_1(x)$ and $h_2(x)$) which are assumed to have the following forms to give some flexibility in control law selection: $h_i(x) = h_{i1}x_1 + h_{i2}x_2 + h_{i3}x_1x_2 + h_{i4}x_1^2 + h_{i5}x_2^2 + h_{i6}x_1x_2^2 + h_{i7}x_1^2x_2 + h_{i8}x_1^3 + h_{i9}x_2^3$, $i = 1, 2$. The parameters a_i, b_i, c_i, and d_i ($i = 1, 2, 3, 4$), h_{1i} and h_{2i}, $i = 1, \ldots, 9$, and v_i, $i = 1, \ldots, 5$, will be decision variables of the optimization problem to be used in selecting parameters for these equations that attempt to meet the theory while satisfying control-theoretic constraints. The vector containing all of these parameters is denoted by $\bar{p}$. The sampling period Δ, level set bounds ρ, ρ_e, ρ_s, and $\rho_{\min}$, and Lipshitz constant L_x' are set as decision variables. The objective function is selected as $10^6\Delta$ and is maximized to attempt to find a sampling period Δ which is large enough to be physically feasible.

The constraints will be based on the requirements in Section 3.1.4; however, these requirements involve various parameters such as M that so far in this work have been determined by evaluating functions at certain points in a discretization of state-space. For this initial algorithm, we will

continue in this fashion. Therefore, some of the constraints will need to be developed such that they hold at certain grid points, and before the optimization problem begins, any parameters used in other constraints that do not depend on the decision variables in the optimization problem (such as M) can be determined using the discretization that will be used in the optimization problem. We will perform this initial algorithm in the absence of disturbances, and M will then be selected before the optimization problem is initiated by checking the value for many different values of x and u and taking the maximum. The discretization used in selecting M was initially taken to be in a relatively small neighborhood of the steady-state, where the range of C_A between 0.75 and 1.75 kmol/m^3 (in increments of 0.5 kmol/m^3) and of T between 435 K and 441 K (in increments of 1 K) were used, with the range of u_1 discretized in units of 1 kmol/m^3 and the range of u_2 discretized in units of 5×10^5 kJ/h. This discretization is coarse; making it finer increases the time to solve the optimization problem. In general in this method, one could attempt to use a tighter discretization for the optimization problem, or to solve the optimization problem with a coarser discretization and then check the results with some finer discretizations to explore whether the parameters identified by the optimization problem seem to be sufficient even with the finer discretization. One of the limitations of this method is that it still relies on making discretizations and checking values at many points, so that if only checks are done of some finite number of points and the theoretical conditions are seen to hold at these, that does not guarantee the absence of any safety vulnerabilities at points not checked.

The constraints that must be added are then broken down into six groups: 1) a constraint set where Eqs. 19a-19d are enforced at each point in the discretization used for obtaining M and with the assumed forms of α_j, $j = 1, \ldots, 4$, h (with saturation at the input bounds), and V (leading to a known form of $\frac{\partial V}{\partial x}$); 2) a second set of constraints that enforce Eq. 20b using the grids for M, with L'_x as a decision variable; 3) a third set of constraints which require that the value of the decision variable ρ be less than the Lyapunov function value at the boundary points of the grid; 4) a fourth set of constraints focused on the conditions in Theorem 1; 5) a fifth set of constraints preventing V or α_j, $j = 1, 2, 3, 4$, from becoming zero; and 6) a sixth set of constraints corresponding to bounds on the decision variables.

We will now provide more details regarding the fourth set of constraints. The first is:

$$\rho_e - \rho \leq 0 \tag{31}$$

and is Eq. 26 when $\theta = 0$ (the no-disturbance case under consideration). The next constraint is Eq. 27 when $\theta = 0$, and assuming $-\epsilon_w/\Delta = -10^{-8}$; however, this equation requires $-\alpha_3(\alpha_2^{-1}(\rho_s))$, when ρ_s and the parameters defining α_3 and α_2 are decision variables. A decision variable $|\bar{x}|$ is defined to represent $\alpha_2^{-1}(\rho_s)$, which is defined by the following equality constraint:

$$b_1|\bar{x}| + b_2(|\bar{x}|)^2 + b_3(|\bar{x}|)^4 - \rho_s = 0 \tag{32}$$

The resulting value of $|\bar{x}|$ is then used in developing the representation of Eq. 27 that is used as a constraint of the optimization problem as follows:

$$-c_1|\bar{x}| - c_2|\bar{x}|^2 - c_3|\bar{x}|^4 + L_x' M\Delta + 10^{-8} \leq 0 \tag{33}$$

The next constraint to be enforced is

$$\rho_s + L_x' M\Delta^2 - \rho_{\min} \leq 0 \tag{34}$$

which is used to separate ρ_s and $\rho_{\min}$ according to Eq. 28 Oyama et al. (2022). Finally, to account for the required hierarchies of level sets ($\rho > \rho_e > \rho_{min}$), a constraint requiring that $\rho_{\min} \leq \rho_e$ is also enforced.

The fifth set of constraints seeks to prevent the optimization problem from setting important functions that should not be zero to zero. Specifically, because V and α_j, $j = 1, 2, 3, 4$, should be positive definite, there are constraints that the sum of the absolute values of the coefficients for each function should be at least 10^{-5}. Regarding bounds on the decision variables, this problem has 42 decision variables corresponding to Δ, ρ, ρ_e, the coefficients of α_1, α_2, α_3, α_4, V, h_1, and h_2, and L_x', ρ_s, $\rho_{\min}$, and $|\bar{x}|$. The bounds on every decision variable are set between 0 and 10^{17}, except for the decision variables corresponding to the parameters of h_1 and h_2, which had lower bounds of -10^{-17} and upper bounds of 10^{17}, and the values of Δ (which was restricted to be in the range 10^{-6} and 1) and ρ (which was restricted to be in the range 10^{-6} to 10^{17}).

This optimization problem was solved using Ipopt with ADOL-C, and the problem may not have solved to global optimality. The initial guesses for the decision variables are presented in Table 7. The constraints were scaled by factors presented in Table 8. The results are presented in Table 9. It is significant that Ipopt was able to find a value of Δ on the order of 10^{-5} h in this case that met the other constraints at the same time, indicating that it may be possible to find a way to set up the problem that puts Δ on a desirable order of magnitude for this problem.

Table 7: Decision Variable Guesses.

Parameter	**Guess**	**Parameter**	**Guess**
Δ	$1.55083162028051 \times 10^{-14}$	h_{11}	-16919.7681573979
ρ	0.00100000000882223	h_{12}	7321.9748676489
ρ_e	0.000988488677936539	h_{13}	4218.46579549029
a_1	$1.53800929247839 \times 10^{-5}$	h_{14}	8028.15761721977
a_2	$4.53010147324655 \times 10^{-5}$	h_{15}	-507.949104979065
a_3	$1.84354586277442 \times 10^{-6}$	h_{16}	-590.931651961331
b_1	0.00800437054717969	h_{17}	-2190.67179605869
b_2	62.2475533226796	h_{18}	-2985.77115185349
b_3	0.00497969280330501	h_{19}	1988.39442155344
c_1	$2.11162515322774 \times 10^{-5}$	h_{21}	21985.9180169341
c_2	$6.79219640525747 \times 10^{-9}$	h_{22}	-22507.31871886
c_3	$6.89032786977831 \times 10^{-9}$	h_{23}	29867.1870814213
d_1	0.00418019308985226	h_{24}	3705.38368144527
d_2	$7.08510412365131 \times 10^{-5}$	h_{25}	88381.9586639903
d_3	46127.6083797397	h_{26}	33895.3546418904
v_1	0.00443314020645772	h_{27}	-1896.06843146131
v_2	0.000131237335333051	h_{28}	6811.45428158675
v_3	$4.15242120294597 \times 10^{-9}$	h_{29}	-116284.529184278
v_4	$3.99459102873933 \times 10^{-12}$	L'_x	1.36151111986363
v_5	$2.98396599046021 \times 10^{-8}$	ρ_s	0.000944774396498493
		$\rho_{\min}$	0.000973690090808806
		$\lvert\bar{x}\rvert$	0.00382965502467688

Several comments on the solution strategy of the optimization problem should be made. It should be noted that the problem in Ipopt was not set up in an ideal fashion for this initial study (for example, there are constraints in which decision variables multiply one another and no attempt has been made to reformulate these to separate them). Future studies could further investigate how to appropriately formulate the problem numerically, but some initial results from this initial setup

Table 8: Constraints with scaling factors.

Constraint	**Scaling Factor**
$\alpha_1(\|x\|) \leq V(x)$	10^6
$V(x) \leq \alpha_2(\|x\|)$	10^{-2}
$\dot{V} \leq -\alpha_3(\|x\|)$	1
$\left\|\frac{\partial V}{\partial x}\right\| \leq \alpha_4(\|x\|)$	10^{-6}
$\left\|\frac{\partial V(x)}{\partial x} f(x,u,0) - \frac{\partial V(x')}{\partial x} f(x',u,0)\right\| \leq L_x^{'}\|x-x'\|$, for x and x' in the state-space discretization and u in the input discretization	1
$\rho_e \leq \rho$	10^5
$-c_1\|\bar{x}\| - c_2\|\bar{x}\|^2 - c_3\|\bar{x}\|^4 + L_x' M\Delta \leq -10^{-8}$	10^8
$\rho_s + L_x' M\Delta^2 \leq \rho_{\min}$	10^5
$\rho_{\min} \leq \rho_e$	10^5
$10^{-5} \leq \|a_1\| + \|a_2\| + \|a_3\|$	10^{-1}
$10^{-5} \leq \|b_1\| + \|b_2\| + \|b_3\|$	10^{-1}
$10^{-5} \leq \|c_1\| + \|c_2\| + \|c_3\|$	10^5
$10^{-5} \leq \|d_1\| + \|d_2\| + \|d_3\|$	10^{-4}
$10^{-5} \leq \|v_1\| + \|v_2\| + \|v_3\| + \|v_4\| + \|v_5\|$	10^3
$\rho \leq V(x)$, for x evaluated at corners of discretization	10^4
$b_1\|\bar{x}\| + b_2(\|\bar{x}\|)^2 + b_3(\|\bar{x}\|)^4 - \rho_s = 0$	10^6

of the problem still enable insights to be gained. Furthermore, it is noted that the formulation that gives the results in Table 9 that seems to be promising for the application of this method was not the initial formulation tried. A number of adjustments were made to the problem to arrive at this final form that gave a non-zero value of Δ as the final answer (for example, adjustments to the bounds on Δ or on the value of the sum of the absolute values of the coefficients of V and α_j, $j = 1, 2, 3, 4$). Therefore, it should be understood that some of these aspects of the optimization problem are tunable for attempting to try to find a solution that is desirable, and also that a desirable solution may not be easy to obtain even with this optimization problem method. Despite this, we consider the ability of this optimization problem to find a solution that appears to satisfy many of the theoretical conditions of an LEMPC for some discretizations of the state-space with a value of Δ that is on a desirable order of magnitude to be a move toward developing better algorithms for simulating an LEMPC with safety guarantees (and, ideally with modifications in future research, safety guarantees in the presence of cyberattacks).

Table 9: Result of optimization problem method.

Parameter	**Value**	**Parameter**	**Value**
Δ	0.00004918924267	h_{11}	-16919.76815739789890
ρ	1544.44280315388846	h_{12}	7321.97486764892983
ρ_e	1544.44279068871106	h_{13}	4218.46579549028957
a_1	42.56134909552156	h_{14}	8028.15761721977015
a_2	36.20947653353708	h_{15}	-507.94910497906494
a_3	4.81813169648454	h_{16}	-590.93165196133100
b_1	0.00208551911091	h_{17}	-2190.67179605868978
b_2	0.00587598357892	h_{18}	-2985.77115185349021
b_3	19081.03953105145774	h_{19}	1988.39442155344000
c_1	884489.10394334455486	h_{21}	257809.49617722025141
c_2	0.00120706296049	h_{22}	-4669419.83828037418425
c_3	0.00012536153193	h_{23}	-59704.79336714102828
d_1	43372348.62285971641541	h_{24}	11834552.60541500523686
d_2	39844692.87630474567413	h_{25}	665396.80664730246644
d_3	73802038.86971308290958	h_{26}	17889.32867738550704
v_1	6810.28698984776020	h_{27}	-2935808.84039304591715
v_2	336.95169942715870	h_{28}	660437.80361377366353
v_3	0.00078855478332	h_{29}	-727484.69599351705983
v_4	0.00000224460841	L'_x	3183363.34428080823272
v_5	0.00000007394288	ρ_s	1521.32385671573297
		$\rho_{\min}$	1544.44277822353365
		$\lvert\bar{x}\rvert$	0.53137939940765

After obtaining a solution to the optimization problem, it is desirable to check via MATLAB whether it satisfies the constraints using the state-space and input space discretizations from the optimization problem. The solution was checked with the discretization of the optimization problem and met the constraints of the optimization problem. This does not provide conclusive evidence that the solution of the optimization problem would continue to meet the theoretical requirements as the discretization was made arbitrarily small, but suggests that the optimization problem may have found a solution that could be used in simulating a process under an LEMPC in a manner that might meet theoretical requirements.

We can compare this optimization-based approach to that in the prior section that involved *a priori* selecting the functions to utilize in the LEMPC and then performing a type of best-case analysis for determining a maximum allowable value of Δ. Either method may give parameters

and functions that, when checked for multiple discretizations of the state and input space, seem to be viable parameters for an LEMPC. The benefit of the optimization strategy compared to the guess-and-check strategy, if the guess-and-check strategy does not yield immediate results, is that it enables a systematic search even for functions that can aid in meeting theoretical requirements for LEMPC with (potentially) industrially-relevant sampling periods. However, it still retains many tuning parameters in the optimization problem for attempting to locate a desirable set of parameters.

The focus of this section was on setting up an optimization problem incorporating many theoretical conditions of LEMPC and seeing whether parameters could be obtained from this method that met a desired operating goal. While it appears that such parameters could be found for this problem (for the discretization used), the study above does not address the performance of an LEMPC under the parameters obtained. When the parameters obtained are utilized in a closed-loop simulation, it is possible that additional behavior will be observed which would have been desirable to constrain in finding the system parameters, or that attempting to utilize the same method for another system may prove challenging. Exploring the translation of this methodology into the full simulation of closed-loop systems can be a subject of future research.

Remark 7. *The computational challenges with searching for the parameters and functions satisfying this control law are not unexpected. In particular, it would be expected that for nonlinear systems, extensive testing of how the control designs may work for robust control is needed (e.g., Mayne et al. (2011)).*

Remark 8. *If it was desired to explore whether ρ could be made larger, one might consider expanding the bounds of the state-space grid and re-running the optimization problem to see if this gives larger values for ρ. One limitation of this method is that it applies the constraints throughout all of the discretization, including those which require, for example, a decrease in $\dot{V}$, which is not in general required everywhere outside of Ω_ρ.*

Remark 9. *One could consider that in addition to maximizing Δ, if many terms are suggested for h, V, or α_j, $j = 1, 2, 3, 4$, it may be desirable to prevent the optimization problem from giving coefficients to all of these if possible (in the spirit of sparse regression inspired by Brunton et al.*

(2016)). Therefore, in the objective function, one could also consider penalizing a weighted norm of the vector of the coefficients of these terms, leading to a multiobjective optimization problem for locating various parameters and functions of LEMPC that can trade off between selecting a larger Δ *and preventing the functions being selected from including every possible term. However, one of the challenges is that in general* Δ *may be very small for satisfying all of the theoretical conditions; trading its maximization off with other terms therefore must be done with care to ensure that the other terms do not receive so much weight in the objective function that undesirable values of* Δ *are selected by the optimizer.*

4. Conclusion

This work explored two concepts related to dynamic process operation and safety. The first was an exploration of the use of computational fluid dynamics (CFD) combined with finite element analysis (FEA) simulation to investigate impacts of process control on design and equipment in the presence of cyberattacks or economic model predictive control. These results showcased the use of such software in evaluating the process as a whole under advanced control and cyberattacks, and showcased how the CFD/FEA data might be used to develop data-driven models that aid in more rapidly screening various dynamic operation scenarios, or in developing control laws that take into account equipment stress models. In the second, we expanded on work performed in Oyama et al. (2022) related to beginning steps toward obtaining parameters of an advanced control law that has been explored in safety and cybersecurity contexts (LEMPC) to seek to better understand how parameters and functions for this control law that meet theoretical conditions might be obtained. Specifically, we indicated the potential difficulty of a guess-and-check approach to obtaining reasonable parameters of an LEMPC such as the sampling period that might meet the theory, and explore the use of optimization as an alternative strategy. Though both strategies may involve degrees of tuning to attempt to locate LEMPC parameters, the optimization technique allows some flexibility in searching for functions and parameters when an initial screening with the guess-and-check approach does not seem to provide desired results.

Acknowledgement

Financial support from the Air Force Office of Scientific Research (award number FA9550-19-1-0059), National Science Foundation CNS-1932026 and CBET-1839675, and Wayne State University is gratefully acknowledged.

Literature Cited

Anderson, J.D., Wendt, J., 1995. Computational fluid dynamics. volume 206. Springer.

ANSYS, 2020a. Ansys fluent 2020 r1 theory guide .

ANSYS, 2020b. Ansys fluent 2020 r1 user's guide .

ANSYS, 2022. Mechanical application 2022 r2 mechanical user's guide .

Behroozinia, P., Khaleghian, S., Taheri, S., Mirzaeifar, R., 2019. Damage diagnosis in intelligent tires using time-domain and frequency-domain analysis. Mechanics Based Design of Structures and Machines 47, 54–66.

Billings, S.A., 2013. Nonlinear system identification: NARMAX methods in the time, frequency, and spatio-temporal domains. John Wiley & Sons.

Brunton, S.L., Proctor, J.L., Kutz, J.N., 2016. Discovering governing equations from data by sparse identification of nonlinear dynamical systems. Proceedings of the National Academy of Sciences 113, 3932–3937.

Byres, E., Lowe, J., 2004. The myths and facts behind cyber security risks for industrial control systems, in: Proceedings of the VDE Kongress, Citeseer. pp. 213–218.

Candell, R., Stouffer, K., Anand, D., et al., 2014. A cybersecurity testbed for industrial control systems, in: Proceedings of the 2014 Process Control and Safety Symposium, pp. 1–16.

Cormier, A., Ng, C., 2020. Integrating cybersecurity in hazard and risk analyses. Journal of Loss Prevention in the Process Industries 64, 104044.

Dermitzakis, I., Kravaris, C., 2009. Higher-order corrections to the pi criterion for the periodic operation of chemical reactors, in: 2009 IEEE Control Applications,(CCA) & Intelligent Control,(ISIC), IEEE. pp. 376–381.

Diehl, M., Amrit, R., Rawlings, J.B., 2010. A Lyapunov function for economic optimizing model predictive control. IEEE Transactions on Automatic Control 56, 703–707.

Ding, D., Han, Q.L., Xiang, Y., Ge, X., Zhang, X.M., 2018. A survey on security control and attack detection for industrial cyber-physical systems. Neurocomputing 275, 1674–1683.

Durand, H., 2019a. On accounting for equipment-control interactions in economic model predictive control via process state constraints. Chemical Engineering Research and Design 144, 63–78.

Durand, H., 2019b. On accounting for equipment-control interactions in economic model predictive control via process state constraints. Chemical Engineering Research and Design 144, 63–78. URL: https://www.sciencedirect.com/science/article/pii/S0263876219300425, doi:https://doi.org/10.1016/j.cherd.2019.01.028.

Durand, H., Wegener, M., 2020. Mitigating safety concerns and profit/production losses for chemical process control systems under cyberattacks via design/control methods. Mathematics 8. URL: https://www.mdpi.com/2227-7390/8/4/499, doi:10.3390/math8040499.

Elliott, J.R., Lira, C.T., Lira, C.T., 2012. Introductory chemical engineering thermodynamics. volume 668. Prentice Hall Upper Saddle River, NJ.

Ellis, M., Christofides, P.D., 2014. Economic model predictive control with time-varying objective function for nonlinear process systems. AIChE Journal 60, 507–519.

Ellis, M., Durand, H., Christofides, P.D., 2014a. A tutorial review of economic model predictive control methods. Journal of Process Control 24, 1156–1178.

Ellis, M., Durand, H., Christofides, P.D., 2014b. A tutorial review of economic model predictive control methods. Journal of Process Control 24, 1156–1178.

Gopalakrishnan, A., Biegler, L.T., 2013. Economic nonlinear model predictive control for periodic optimal operation of gas pipeline networks. Computers & Chemical Engineering 52, 90–99.

Griffith, D.W., 2018. Advances in Nonlinear Model Predictive Control for Large-Scale Chemical Process Systems. Ph.D. thesis. Carnegie Mellon University.

Griffith, D.W., Zavala, V.M., Biegler, L.T., 2017. Robustly stable economic nmpc for non-dissipative stage costs. Journal of Process Control 57, 116–126.

Heidarinejad, M., Liu, J., Christofides, P.D., 2012. Economic model predictive control of nonlinear process systems using Lyapunov techniques. AIChE Journal 58, 855–870.

Khorrami, F., Krishnamurthy, P., Karri, R., 2016. Cybersecurity for control systems: A process-aware perspective. IEEE Design & Test 33, 75–83.

Kim, R., Lima, F.V., 2022. Nonlinear multiobjective and dynamic real-time predictive optimization for optimal operation of baseload power plants under variable renewable energy. Optimal Control Applications and Methods .

Lao, L., Aguirre, A., Tran, A., Wu, Z., Durand, H., Christofides, P.D., 2016. Cfd modeling and control of a steam methane reforming reactor. Chemical Engineering Science 148, 78–92.

Latham, D.A., McAuley, K.B., Peppley, B.A., Raybold, T.M., 2011. Mathematical modeling of an industrial steam-methane reformer for on-line deployment. Fuel processing technology 92, 1574–1586.

Lin, Y., Sontag, E.D., 1991. A universal formula for stabilization with bounded controls. Systems & Control Letters 16, 393–397.

Mahoney, T. C. ed., D.J., 2017. Cybersecurity for manufacturers: Securing the digitized and connected factory. Report No. MF-TR-2017-0202, MForesight: Alliance for Manufacturing Foresight and Computing Research Association's Computing Community Consortium .

Mayne, D.Q., Kerrigan, E.C., Van Wyk, E., Falugi, P., 2011. Tube-based robust nonlinear model predictive control. International journal of robust and nonlinear control 21, 1341–1353.

Meesala, V.C., Ragab, S., Hajj, M.R., Shahab, S., 2020. Acoustic-electroelastic interactions in ultrasound energy transfer systems: Reduced-order modeling and experiment. Journal of Sound and Vibration 475, 115255.

Mhaskar, P., Liu, J., Christofides, P.D., 2012. Fault-tolerant process control: methods and applications. Springer Science & Business Media.

Müller, M.A., Grüne, L., 2016. Economic model predictive control without terminal constraints for optimal periodic behavior. Automatica 70, 128–139.

Nieman, K., Oyama, H.C., Wegener, M., Durand, H., 2020. Predict the impact of cyberattacks on control systems. Chemical Engineering Progress 116, 52–57.

Oyama, H., Durand, H., 2020a. Integrated cyberattack detection and resilient control strategies using lyapunov-based economic model predictive control. AIChE Journal 66, e17084.

Oyama, H., Durand, H., 2020b. Interactions between control and process design under economic model predictive control. Journal of Process Control 92, 1–18.

Oyama, H., Messina, D., Rangan, K.K., Durand, H., 2022. Lyapunov-based economic model predictive control for detecting and handling actuator and simultaneous sensor/actuator cyberattacks on process control systems. Frontiers in Chemical Engineering 4, 810129.

Oyama, H., Rangan, K.K., Durand, H., 2021. Handling of stealthy sensor and actuator cyberattacks on evolving nonlinear process systems. Journal of Advanced Manufacturing and Processing 3, e10099.

Perales Gomez, A.L., Fernández Maimó, L., Huertas Celdran, A., Garcia Clemente, F.J., Gil Pérez, M., Martínez Pérez, G., 2021. Safeman: A unified framework to manage cybersecurity and safety in manufacturing industry. Software: Practice and Experience 51, 607–627.

Rangan, K.K., Oyama, H., Durand, H., 2021. Integrated cyberattack detection and handling for nonlinear systems with evolving process dynamics under lyapunov-based economic model predictive control. Chemical Engineering Research and Design 170, 147–179.

Rhinehart, R.R., 2016. Nonlinear regression modeling for engineering applications: modeling, model validation, and enabling design of experiments. John Wiley & Sons.

Silveston, P.L., 1987. Periodic operation of chemical reactors-a review of the experimental literature. Sadhana 10, 217–246.

Steel Founders' Society of America, 2004. Steel castings handbook supplement 9 high alloy data sheets heat series. Steel Founders' Society of America .

Tran, A., Aguirre, A., Durand, H., Crose, M., Christofides, P.D., 2017a. Cfd modeling of a industrial-scale steam methane reforming furnace. Chemical Engineering Science 171, 576–598.

Tran, A., Aguirre, A., Durand, H., Crose, M., Christofides, P.D., 2017b. CFD modeling of a industrial-scale steam methane reforming furnace. Chemical Engineering Science 171, 576–598.

Tuptuk, N., Hailes, S., 2018. Security of smart manufacturing systems. Journal of Manufacturing Systems 47, 93–106.

Wächter, A., Biegler, L.T., 2006. On the implementation of an interior-point filter line-search algorithm for large-scale nonlinear programming. Mathematical programming 106, 25–57.

Walther, A., 2010. source:trunk/adol-c/examples/additional_examples/ipopt/mittelmanndistcntrlneuma@78. `https://projects.coin-or.org/ADOL-C/browser/trunk/ADOL-C/examples/additional_examples/ipopt/MittelmannDistCntrlNeumA?rev=78`.

Walther, A., Griewank, A., 2009. Getting started with ADOL-C. Combinatorial Scientific Computing , 181–202.

Wang, Y., Bhattacharyya, D., Turton, R., 2019. Evaluation of novel configurations of natural gas

combined cycle (ngcc) power plants for load-following operation using dynamic modeling and optimization. Energy & Fuels 34, 1053–1070.

Webb, G.M., Taylor, W., 2007. Reformer tubes: Not a commodity. Process safety progress 26, 159–163.

Wells, L.J., Camelio, J.A., Williams, C.B., White, J., 2014. Cyber-physical security challenges in manufacturing systems. Manufacturing Letters 2, 74–77.

Wiebe, J., Cecílio, I., Misener, R., 2018. Data-driven optimization of processes with degrading equipment. Industrial & Engineering Chemistry Research 57, 17177–17191.

Wu, D., Ren, A., Zhang, W., Fan, F., Liu, P., Fu, X., Terpenny, J., 2018. Cybersecurity for digital manufacturing. Journal of manufacturing systems 48, 3–12.

Xu, J., Froment, G.F., 1989. Methane steam reforming, methanation and water-gas shift: I. intrinsic kinetics. AIChE journal 35, 88–96.